Evaluation of temperature history of a spherical nanosystem irradiated with various short-pulse laser sources

Arnab Lahiri[1] and Pranab K. Mondal[2,*]

[1]*School of Mechanical Engineering, Kalinga Institute of Industrial Technology, Bhubaneswar 751024, India*

[2]*Department of Mechanical Engineering, Indian Institute of Technology Guwahati, Guwahati 781039, India*

(Received 24 December 2017; published 9 April 2018)

Spatiotemporal thermal response and characteristics of net entropy production rate of a gold nanosphere (radius: 50–200 nm), subjected to a short-pulse, femtosecond laser is reported. In order to correctly illustrate the temperature history of laser-metal interaction(s) at picoseconds transient with a comprehensive single temperature definition in macroscale and to further understand how the thermophysical response of the single-phase lag (SPL) and dual-phase lag (DPL) frameworks (with various lag-ratios') differs, governing energy equations derived from these benchmark non-Fourier frameworks are numerically solved and thermodynamic assessment under both the classical irreversible thermodynamics (CIT) as well as extended irreversible thermodynamics (EIT) frameworks is subsequently carried out. Under the frameworks of SPL and DPL with small lag ratio, thermophysical anomalies such as temperature overshooting characterized by adverse temperature gradient is observed to violate the local thermodynamic equilibrium (LTE) hypothesis. The EIT framework, however, justifies the compatibility of overshooting of temperature with the second law of thermodynamics under a nonequilibrium paradigm. The DPL framework with higher lag ratio was however observed to remain free from temperature overshooting and finds suitable consistency with LTE hypothesis. In order to solve the dimensional non-Fourier governing energy equation with volumetric laser-irradiation source term(s), the lattice Boltzmann method (LBM) is extended and a three-time level, fully implicit, second order accurate finite difference method (FDM) is illustrated. For all situations under observation, the LBM scheme is featured to be computationally superior to remaining FDM schemes. With detailed prediction of maximum temperature rise and the corresponding peaking time by all the numerical schemes, effects of the change of radius of the gold nanosphere, the magnitude of fluence of laser, and laser irradiation with multiple pulses on thermal energy transport and lagging behavior (if any) are further elucidated at different radial locations of the gold nanosphere. Last, efforts are further made to address the thermophysical characteristics when effective thermal conductivity (with temporal and size effects) is considered instead of the usual bulk thermal conductivity.

DOI: 10.1103/PhysRevE.97.043302

I. INTRODUCTION

No natural phenomenon proceeds in nature instantaneously with infinite velocity of propagation of disturbance. Heat transfer further adds no exception to this constraint. Investigations and applications in small spatiotemporal scale are not analyzed by the same principles and methodologies that govern situations defined in macroscale [1–5]. With rapid development of short-pulse lasers (with pulse duration as small as a femtosecond), thermal interaction of laser pulse with micro- or nanoscale metallic spatial domain (submicron), and further analysis of thermal response at small (picoseconds) temporal domain has gained significant attention from the research community accounting for its huge applications in past decades [1–7]. Characterized by nonequilibrium transition of thermal energy, deviation of these problems from the macroscopic quasiequilibrium thermodynamic transition are well realized on account of a few facets as follows: extremely short laser pulse duration ($\sim 10^{-15}$ s) leading to response time shorter than the corresponding relaxation time as well as nonequilibrium transition of thermal energy through an extremely small spatial domain of the order of mean-free-path of phonon-electron collision ($\sim 10^{-9}$ m) during laser-material interaction(s). Therefore, energy interaction(s) and transport phenomena at these small spatial and temporal domains are not thermophysically emulated by the classical phenomenological diffusion energy equation (derived from Fourier's law of heat conduction).

The mathematical frameworks employed to depict transport phenomena should promise to properly address the associated microscopic effects both in space and time. Among numerous microscopic (two-step models) approaches reported and deployed in literature [1–5] to address the thermophysical characterization(s), for example the two-step model by Qiu and Tien [2,3] for radiation-metal interactions and the semiclassical two-temperature model by Chen *et al.* [4,5] for ultrafast transient laser heating, had proved to become accurate, evidenced by established experimental observations (Brorson *et al.* [6] and Qiu *et al.* [7]) as well. Dependent variables, described by the corresponding two-step frameworks are, however, microscopic and do not find suitable interpretation under the scope of local thermodynamic equilibrium (LTE),

*Corresponding author: mail2pranab@gmail.com; pranabm@iitg.ernet.in

continuum, or macroscale. Since applications in practice demand appropriate macroscopic meaning, investigations at the micro- or nanoscale range demand suitable interpretation(s) in macroscale without any generalized loss or compromise with the related physics. The single-phase-lag framework (SPL) [8,9] was initially developed conceiving the fact that heat flux is established in continuum only after the relaxation time, whereas temperature gradient is established instantaneously in the physical domain. Unlike classical diffusion (the governing energy equation derived from Fourier's law of heat conduction), this framework (SPL) circumvents the infinite velocity of thermal wave propagation predicted by the former and results in consideration of finite thermal wave speed, expected to manifest at small (picoseconds) time domain with the possibility of encompassing microscale response in time. Though SPL framework (Cattaneo's equation) can be derived from Boltzmann transport equation [10] and higher-order continuum transport equations [11], consistency with the second law of thermodynamics was, however, not ascertained.

Wave behavior at picoseconds time domain further implies a thermal penetration depth of the order of micro- or nanometers. Hence, heat transfer through a material domain of the order of micro- or nanometer in the short-time (picosecond) time domain must physically encompass the microscopic spatial interaction(s), which remains beyond the capability of the SPL framework [3]. This leads to the unlikeness of the SPL framework with widely validated two-step models [2–5] that considers the microscopic interactions of energy carriers (phonon-electron, phonon-phonon, etc.) in space. Experimentally, sharp thermal waves (with discontinuities) predicted by the SPL framework were not witnessed within any metallic domain during the picosecond response time of heating. The dual-phase-lag heat conduction model (DPL) proposed by Tzou [12], on the other hand, had fetched adequate attention in the past three decades for generalizing the SPL framework and providing a consistent macroscopic approach by considering the microscopic interactions in time as well as in space. Incorporation of microscopic spatiotemporal effects in the macroscopic scale as a delayed thermal response [12] formulates the DPL governing equation as

$$\bar{q}(\bar{r},t+\tau_q) = -k\nabla T(\bar{r},t+\tau_T). \tag{1}$$

In Eq. (1) τ_q is the time lag (relaxation) of heat flux and τ_T is the time lag (thermalization) of temperature gradient. Note that Eq. (1) physically signifies that if the energy equation is written at a time instant t, development of heat flux and temperature gradient is shifted in continuum at a time instant of $(t+\tau_q)$ and $(t+\tau_T)$ respectively. Tzou [12] described τ_q and τ_T as intrinsic properties of the medium. It may be mentioned here that τ_T is described to capture the microscopic effects in space (on account of phonon-electron interaction or phonon scattering) defined to be as the finite time required to increase the temperature of metal lattice by 1°. The wavelike behavior of temperature is pronounced for $\tau_T < \tau_q$ and further reduced to the SPL (wave) framework for $\tau_T \to 0$. Similarly, $\tau_q > \tau_T$ is characterized by diffusionlike behavior of temperature and further reduced to classical diffusion framework when $\tau_q = \tau_T$ or $\tau_q = \tau_T = 0$. Hence, with a comprehensive single temperature definition and intrinsic (lagging) properties of material shifting the spatiotemporal microscopic interactions to a delayed thermal response in macroscale, the DPL or SPL framework(s) is professed as a fancy macroscopic model. As addressed by these non-Fourier frameworks, accountability of macroscopic interpretation(s) of this microscopic phenomenon (ultrafast transient heating of nanoscale metallic domain) brings the rudimentary question(s) of qualitative attributes of macroscopic "single temperature" defined by them. A convincing explanation can, however, be addressed by the second law of thermodynamics.

Interaction of short-pulse laser application with gold (Au) nanoparticles or nanoshells has found profound importance in biomedical applications because of their ability to absorb electromagnetic energy on a scale much smaller than the wavelength of incident radiation [13] and the thermophysical properties of gold (Au) nanoparticles or nanoshells appear to be compatible with biomacromolecules [13,14]. During noninvasive laser photothermal therapy for cancer treatment, ability of gold nanoparticles to absorb laser irradiation and its successive conversion to heat results in a negligible photothermal destruction of neighboring nonmalignant cells [14]. Other than biomedical applications, considerable importance of short-pulse nanoparticles is well realized in microtechnology [15] as well as in manufacturing applications like selective laser sintering (SLS) [16,17]. In all the above applications, the importance of prediction of the correct temperature distribution in small (picosecond) time transient during interaction of a gold nanosphere (GNS) with a short-pulse, femtosecond laser is well recognized. In order to retrieve the correct macroscopic temperature history in subpicoseconds transient, SPL and furthermore DPL framework(s) are employed. However, governing energy equations for a GNS are required to be solved in spherical coordinate geometry [15]. Unlike problems formulated on the Cartesian coordinate system, solution tools employed to analyze laser-material interaction in axisymmetric (cylindrical and spherical) geometry must be capable of handling two important issues as follows: the first is the additional terms appearing on the energy equation and the second is the singularity witnessed at the center when the corresponding geometry is modeled to be a solid axisymmetric system (instead of considering a hollow one). Previous investigations performed to solve the DPL governing equation for axisymmetric geometries include the analytical solution [18,23], the hybrid application of Laplace transform [19–22], the finite or control volume method [23–25], the finite difference method [15,26–30], and the lattice Boltzmann method [29,30]. In the present study, the LBM scheme has been extended and, furthermore, one implicit FDM scheme is reported to solve the dimensional DPL governing energy equation (for spherical coordinate geometry) with laser irradiation (volumetric) source terms. The new FDM scheme has improvised the local accuracy of time of the FDM [29–31] and inherits second order accuracy (both locally as well as globally) in time and space. All results from these three schemes are validated against the results obtained from the three-level, convergent FDM scheme provided by Dai *et al.* [15]. Furthermore, under the present scope, numerical assessments of four numerical schemes are provided in terms of accuracy, computational time, and convergence characteristics.

Numerous past investigations under SPL or DPL frameworks had revealed the presence of certain thermophysical anomalies for, e.g., evidence of a higher interior temperature

of the physical domain compared to the temperature of irradiated surface (boundary) [29,32–37]. This phenomenon of overshoot of temperature becomes contradictory to the directional constraint of heat transfer (from higher to lower temperature) imposed by the second law of thermodynamics under the macroscopic (continuum) framework. Xu *et al.* [32] investigated the overshooting phenomenon on account of thermal wave interference on the DPL model. Jou *et al.* [33] provided the thermodynamic stability analysis of the DPL framework in the context of the limiting condition of initial temperature rate. Mishra *et al.* [34] performed a numerical experiment to study the effect of the Fourier number and lag ratio on overshooting. The influence of size effect and boundary conditions on temperature overshoot was studied by Li *et al.* [35]. For a thin layer of metallic material, the influence of initial conditions of the first and second rate of change of temperature on overshooting was studied by Al-Nimr *et al.* [36]. All these studies were however, limited to planar geometry. For axisymmetric geometries, Lin and Chen [37] reported the presence of overshoot of temperature during the propagation reflection of thermal waves from a hollow cylinder and sphere when inner and outer boundary is perturbed. With the perturbation of the outer surface, for one-dimensional (1D) cylindrical and spherical geometries under the DPL framework, Mishra *et al.* [25] reported the presence of overshooting of temperature for a small lag ratio. However, qualitative explanations based on the aspects of thermodynamics were not highlighted. The key questions associated with overshooting, witnessed within the interior of any physical domain (subjected to laser irradiation at the surface) are (i) does the directional sense of heat, transferred from the surface to the interior (i.e., from low to high temperature) find any feasible thermodynamic meaning? (ii) Does location(s) prone to temperature overshoot result in a non-negative entropy production rate at any instant of time? And, last, (iii) what does the "single temperature" definition of SPL or DPL physically (macroscopically) signify if the LTE hypothesis is violated? In the context of a solid, spherical coordinate geometry, exposed to short-pulse laser irradiation on the surface, we have tried to answer these questions by first studying the sense (direction) of local heat flux distribution at various instants of time and further by investigating the spatiotemporal net entropy production rate calculated from the classical irreversible thermodynamics (CIT) framework. If investigations under any of these non-Fourier frameworks (SPL and DPL) at any location and time violates the CIT framework [yields negative net (equilibrium) entropy production rate] then, based on the extended irreversible thermodynamics (EIT) framework, further thermodynamic assessment is carried out. Under the EIT framework, certain thermodynamic properties like entropy and temperature are redefined [33,38–41] with a numerical difference between equilibrium and nonequilibrium temperature (if any) estimated.

Once the accuracy of numerical schemes is ascertained and the qualitative aspect(s) of the temperature retrieved from the SPL or DPL framework is well judged, we further employ the numerical schemes to study the thermal characteristics when a GNS is irradiated with multiple series of laser pulses and pulse train respectively. Subjected to different sources, the effect of variation of laser fluence on temperature response was further highlighted. Previously Tzou [42,43] studied the effect of size of the physical domain (thickness) on heat transport, lagging behavior, and peaking time at various locations of the gold film(s) of small microrange thickness. We would like to add here that variation of temperature and normalized heat flux distribution with time at different locations in gold film with laser pulse was reported by Ramadan *et al.* [44]. We here make an effort to understand the (i) transportation of thermal energy and, (ii) characteristics of thermal lagging within the interior of a solid GNS (from surface to the center) with radius varying from 50 to 200 nm, illuminated by various short-pulse(s) laser irradiation. Since the change of absolute temperature is a more important physical index than absolute temperature itself during picoseconds temporal domain [42,43], normalized temperature (reflectivity) change with time is depicted for various radial locations. For completeness, maximum temperature rise (surface) and the corresponding peaking time for all situations studied are elaborately elucidated.

II. FORMULATION

The GNS under consideration is irradiated with a femtosecond short-pulse laser with a range of wavelength varying from the UV to near IR region [2]. Interaction of the laser pulse with a highly conducting, optically opaque GNS results in manifestation of temperature gradient in the radial direction, and thereby heat transfer eventually by conduction. Under this scenario, the response time of the GNS is O (ps) comparable to its relaxation times τ_q and τ_T [12,42–43]. On account of laser-metal interaction, because of a very intense attenuation coefficient (10^5-10^6 cm^{-1}) [45], the laser beam gets absorbed in a very thin layer on the surface (10–30 nm). Typically, it is characterized by the optical (radiation) penetration depth δ which is 15.3 nm for the given case [2–5,15,17,43,45].

It is to be noted that the laser beam radius (0.1–0.3 mm) is much larger than the radius (50–200 nm) of the GNS under considerations [3,17]. For numerous practical applications [13–17], on account of the presence of the surrounding medium (several other nanoparticles or tissues), multiple scattering of radiation leads to a nearly homogeneous distribution of heat flux within the optically penetrated layer [17]. Hence the surface of the GNS in the 4π spherical space receives laser irradiation uniformly with almost normal incidence [Fig. 1(a)] and thereby resulting temperature variations, taking place only in the radial direction, and the problem therefore turns out to be spatially 1D.

For a larger physical domain, optical penetration depth is negligible as compared to the size of the domain, and laser irradiation on the metal surface is generally modelled as a surface source [45]. But for domain of the order of nanometers, the optical penetration depth is not insignificantly small compared to the radius of the GNS. Further, the irradiation of short-pulse laser with the outer surface of the GNS in a very small time scale results in deposition of thermal (radiation) energy from surface to optical penetration depth [3]. Under these circumstances, laser irradiation is considered volumetric where the energy deposited by laser is absorbed by the medium (GNS) and further decayed exponentially from the surface towards the center following Beer's law [46]. With $u(r,t)$ as the locally characterized specific internal energy, and $g(r,t)$ as the volumetric energy deposition rate in the GNS caused by

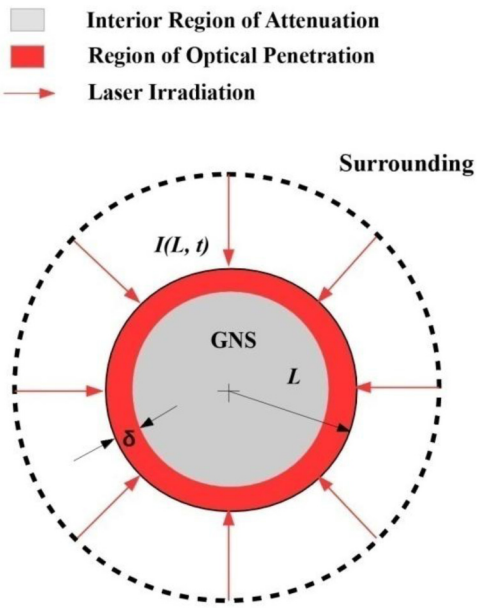

FIG. 1. Physical representation of the problem.

laser irradiation, the energy balance equation is written as

$$\rho\frac{\partial u(r,t)}{\partial t} = \rho c\frac{\partial T(r,t)}{\partial t} = -\frac{1}{r^2}\frac{\partial[r^2 q(r,t)]}{\partial r} + g(r,t) = -\left(\frac{2}{r}q(r,t) + \frac{\partial q(r,t)}{\partial r}\right) + g(r,t). \quad (2)$$

It is important to note that on account of the consideration of a small material domain and the shortening of response time; the physical phenomenon at this small spatiotemporal scale is generally characterized by nonequilibrium transition of thermal energy. In other words, local thermodynamic equilibrium is questionable and subjected to investigation of entropy generation characteristics. In order to circumvent this difficulty, temperature is defined from a generalized notion. In Eq. (1) and further in the entire article, $T(r,t)$ is the generalized absolute temperature. Qualitative meaning of $T(r,t)$ is well realized only after studying the characteristics of the net entropy production rate under equilibrium and nonequilibrium (if required) situations.

Expansion of both the left- and right-hand side terms of Eq. (1) up to first order accuracy by Taylor series, neglecting higher order terms, results in

$$q(r,t) + \tau_q\frac{\partial q(r,t)}{\partial t} = -k\frac{\partial}{\partial r}\left(T(r,t) + \tau_T\frac{\partial T(r,t)}{\partial t}\right). \quad (3)$$

Substitution of q from Eq. (3) into Eq. (2) yields the governing energy equation

$$\rho c\left(\frac{\partial T}{\partial t} + \tau_q\frac{\partial^2 T}{\partial t^2}\right) = \frac{k}{r^2}\frac{\partial}{\partial r}\left[r^2\left(\frac{\partial T}{\partial r} + \tau_T\frac{\partial^2 T}{\partial r\partial t}\right)\right] + G(r,t), \quad (4)$$

where $G(r,t)$ is the overall source term and can be expressed as

$$G(r,t) = \left(g(r,t) + \tau_q\frac{\partial g(r,t)}{\partial t}\right). \quad (4a)$$

Operating the radial derivative $\frac{\partial}{\partial r}$ on the first term on the right-hand side of Eq. (4) gives the nonconservative form of the corresponding DPL governing energy equation with laser irradiation source term,

$$\underbrace{\rho c\frac{\partial T}{\partial t}}_{\text{I}} + \underbrace{\rho c\tau_q\frac{\partial^2 T}{\partial t^2}}_{\text{II}} = \underbrace{\frac{k}{r^2}\frac{\partial}{\partial r}\left(r^2\frac{\partial T}{\partial r}\right)}_{\text{III}} + \underbrace{\frac{2k\tau_T}{r}\frac{\partial^2 T}{\partial r\partial t}}_{\text{IV}} + \underbrace{k\tau_T\frac{\partial^3 T}{\partial r^2\partial t}}_{\text{V}} + G(r,t). \quad (5)$$

In addition to a second order term in both time (term II) and space (term III), i.e., a diffusion term, the governing energy equation [Eq. (5)] contains one second order mixed derivative (term IV) and one third order mixed derivative (term V). The problem is mathematically closed with two initial and two boundary conditions. Initially, the temperature of the GNS is uniform and constant throughout and is equal to the temperature of its surroundings ($T_0 = 300$ K), i.e., $T(r,0) = T_o$. We further assume that no initial rate of heating or cooling was imposed on the GNS which further leads to the second initial condition as $\frac{\partial T(r,0)}{\partial t} = 0$.

As it is explained that the GNS surface receives laser irradiation uniformly at its surface thermally for all time t (on account of isotropic scattering from the surrounding media), temperature distribution is symmetric about its center ($r = 0.0$) [29,30,48]. This physical explanation supports to circumvent the singularity at center ($r = 0.0$). Since the investigation time is very short, the temperature gradient at the outer surface ($r = L$) is negligible [2–5,29–31,33]. This leads to the development of adiabaticlike situations both at the center ($r = 0$) and outer surface ($r = L$) of the GNS. With justifications as above, initial and boundary conditions of temperature and heat flux are summarized as follows.

Initial conditions:

$$T(r,0) = T_o, \quad \frac{\partial T(r,0)}{\partial t} = 0, \quad q(r,0) = 0. \quad (5a)$$

Boundary conditions:

$$\frac{\partial T(0,t)}{\partial r} = 0, \quad \frac{\partial T(L,t)}{\partial r} = 0, \quad q(0,t) = 0, \quad q(L,t) = 0. \quad (5b)$$

After the incident of laser pulse on the outer layer of the GNS, penetration and attenuation of incident radiation take place within the interior of the metal (participating) medium. The effect of volumetric scattering is considered negligible compared to absorption, throughout the mathematical modeling. With $I(L,t)$ as the magnitude of incident laser irradiation at the outer surface of the GNS, irradiation at any radial location r at any instant time t is decayed exponentially, according to

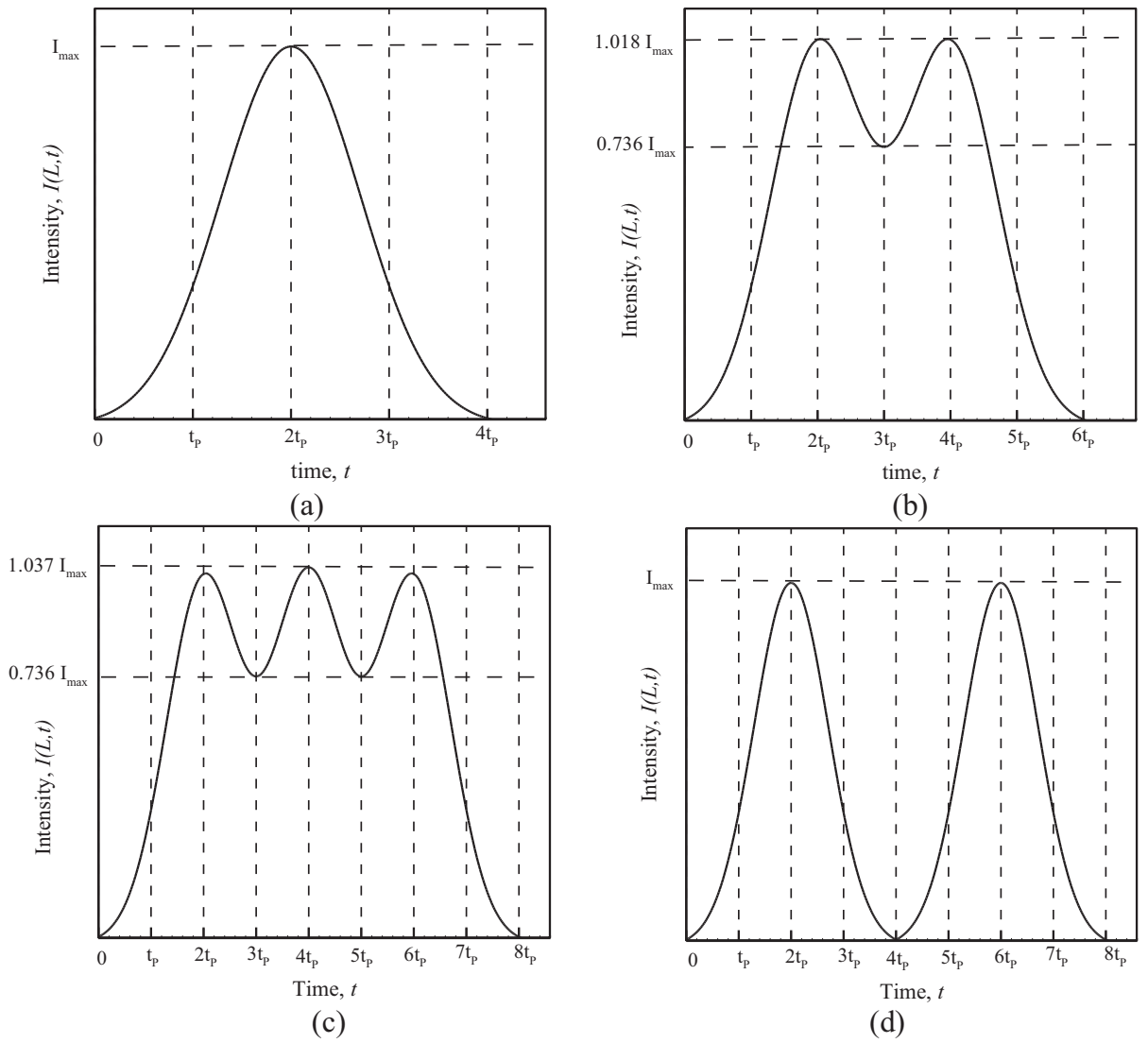

FIG. 2. Temporal intensity distribution of (a) one Gaussian pulse, series of (b) two, (c) three Gaussian laser pulses, and (d) Gaussian laser pulse train.

Beer's law as follows [48]:

$$I(r,t) = I(L,t)\exp\{-\mu_a(L-r)\} = I(L,t)\exp\left(-\frac{L-r}{\delta}\right), \tag{6}$$

where μ_a is the linear absorption coefficient and δ is the optical penetration depth and they are further inversely equal to each other, ($\mu_a = \frac{1}{\delta}$) [45]. In Eq. (6), irradiation received by the GNS surface at any instant of time $I(L,t)$ is modeled to be temporally Gaussian, elucidated as follows:

$$I(L,t) = \sqrt{\frac{\beta}{\pi}}\frac{J}{t_p}\exp\left\{-\beta\left(\frac{t-2t_p}{t_p}\right)^2\right\}. \tag{7}$$

In Eq. (7), J is the laser fluence defined as the total energy delivered by the laser pulse per unit laser spot cross sectional area, R is the reflectivity of the GNS, β is a constant, and t_p is the half width at full maximum (HWFM) of the Gaussian pulse. Following Eq. (7), the peak of the single Gaussian pulse is witnessed at $t = 2t_p$. With the passage of time ($t \geqslant 2t_p$), following the temporal profile of pulse presented in Eq. (7), $I(L,t)$ is observed to decay exponentially with time. The volumetric energy deposition rate $g(r,t)$ in the GNS resulting from the irradiation of a single pulse is given by [2–5,42,43,45]

$$\begin{aligned} g(r,t) &= \{(1.0-R)\mu_a I(r,t) + l(r,t)\} \\ &= \left\{\left(\frac{(1.0-R)I(r,t)}{\delta}\right) + l(r,t)\right\} \\ &= \left[\sqrt{\frac{\beta}{\pi}}\frac{(1.0-R)}{t_p\delta}\,J\,\exp\left\{-\beta\left(\frac{t-2t_P}{t_P}\right)^2\right\}\right. \\ &\quad \left.\times\,\exp\left(-\frac{L-r}{\delta}\right) + l(r,t)\right], \end{aligned} \tag{8}$$

where R is the reflectivity of the gold surface and $l(r,t)$ is the source term on account of phase changes or chemical reaction (if any). Following previous studies [2–5,15,17,28,42,43], in the present work, magnitudes of J R β, and $2t_p$ are adapted as 13.4 (J/m^2), 0.93, 4 ln 2, and 0.2 ps, respectively. The source

term on account of phase changes or chemical reaction is not considered throughout the study. In the present work, effects of irradiation of multiple pulses are also considered. With two consecutive pulses separated by $t = 2t_p$, for p, the number of pulses in series, the temporal incident laser irradiation $I(L,t)$ (at the GNS surface) can be represented by [47]

$$I(L,t) = \left(\sqrt{\frac{\beta}{\pi}}\frac{J}{t_p}\right)\sum_{i=1}^{p}\exp\left\{-\beta\left(\frac{t-2it_p}{t_p}\right)^2\right\}. \quad (9)$$

Here, we have presented results and discussion up to three series of pulses. Further, effect of another pulse train is also reported where peaks of two consecutive pulses are separated by $t = 4t_p$. The temporal incident irradiation $I(L,t)$ (at the GNS surface) in this case can be presented by

$$I(L,t) = \left(\sqrt{\frac{\beta}{\pi}}\frac{J}{t_p}\right)\times\begin{bmatrix}\exp\left\{-\beta\left(\frac{t-2t_p}{t_p}\right)^2\right\}, & 0 \leqslant t < 4t_p\\ \exp\left\{-\beta\left(\frac{t-6t_p}{t_p}\right)^2\right\}, & t \geqslant 4t_p\end{bmatrix}. \quad (10)$$

The profile of the temporal incident irradiation $I(L,t)$ at the GNS surface for all the cases (single pulse, series of two pulses, series of three pulses, and pulse train) are depicted in Fig. 2.

A. Hybrid lattice Boltzmann method formulation (LBM)

Previously Mishra *et al.* [29] reported the application of the LBM scheme to solve the nondimensional radial DPL governing equation for 1D axisymmetric (cylindrical and spherical) geometries without a volumetric source term. In this study, we have extended the application of this scheme to study the thermophysical characteristics of a GNS, irradiated by femtosecond laser pulse(s) under the DPL or SPL framework.

Towards the solution of Eq. (5), it is appreciably noted that it contains (i) second order derivatives of time and space, (ii) second and third order mixed derivatives of time and space, and finally (iii) the spatially and temporally varying source term (short-pulse laser irradiation). The Boltzmann transport equation, on the other hand, contains only the first order derivatives of time and space and a nonlinear collision operator, expressed as follows:

$$\frac{\partial f_i(\bar{r},t)}{\partial t} + \bar{e}_i\cdot\nabla f_i(\bar{r},t) = \Omega_i. \quad (11)$$

In Eq. (11), e_i is the velocity and Ω_i is the collision operator corresponding to the ith particle distribution function (PDF), f_i. Applying the BGK approximation [49], Eq. (11) can be further linearized to obtain the following kinetic LBM formulation with $f_i^{(0)}$ as the equilibrium PDF:

$$f_i(\bar{r}+\bar{e}_i\Delta t,t+\Delta t) - f_i(\bar{r},t) = \omega\left[f_i(\bar{r},t) - f_i^{(0)}(\bar{r},t)\right], \quad (12)$$

where $\omega = -(\frac{\Delta t}{\tau})$ and τ is the relaxation time. In order to encompass all the attributes of the original DPL-transport (energy) equation [Eq. (5)], the volumetric source term (Ψ) can be incorporated in Eq. (12) as follows:

$$\begin{aligned} &f_i(\bar{r}+\bar{e}_i\Delta t,t+\Delta t) - f_i(\bar{r},t)\\ &\quad= \omega\left[f_i(\bar{r},t) - f_i^{(0)}(\bar{r},t)\right] + \Delta t\,\psi_i(\bar{r},t). \end{aligned} \quad (13)$$

$\psi(\bar{r},t)$ must include the presence of (i) the second order temporal derivative of $T(\bar{r},t)$, (ii) additional terms on account of axisymmetric (spherical) geometry, and (iii) the presence of volumetric energy deposition rate $g(\bar{r},t)$, on account of laser pulse(s) irradiating the GNS, in the DPL governing equation [Eq. (8)]. Following previous studies [15–18], $\psi(\bar{r},t)$ can be formulated as follows:

$$\begin{aligned} \psi(\bar{r},t) = {} & A_1\left(\frac{\partial T(\bar{r},t)}{\partial t}\right) + A_2\frac{1}{r}\left(\frac{\partial T(\bar{r},t)}{\partial r}\right)\\ & + A_3\frac{1}{r}\left(\frac{\partial f(\bar{r},t)}{\partial r}\right) + \varphi(\bar{r},t). \end{aligned} \quad (14)$$

Equation (14) contains the first order temporal term (I) and a spatial derivative term (II) of $T(\bar{r},t)$, the spatial derivative term (III) of $f(\bar{r},t)$, and finally the dimensional source term $\varphi(\bar{r},t)$ to encompass the volumetric laser irradiation source term in Eq. (5), for the ith entity. From Eqs. (13) and (14), the governing LBM formulation for the ith particle distribution functions, corresponding to the DPL governing equation [(Eq. (5)], is written as

$$\begin{aligned} &f_i(\bar{r}+\bar{e}_i\Delta t,t+\Delta t) - f_i(\bar{r},t)\\ &= \omega\left[f_i(\bar{r},t) - f_i^{(0)}(\bar{r},t)\right] + \Delta t\left(\underbrace{A_1\left(\frac{\partial T(\bar{r},t)}{\partial t}\right)_i}_{\text{I}} + \underbrace{A_2\frac{1}{r}\left(\frac{\partial T(\bar{r},t)}{\partial r}\right)_i}_{\text{II}} + \underbrace{A_3\frac{1}{r}\left(\frac{\partial f_i(\bar{r},t)}{\partial r}\right)}_{\text{III}} + \varphi_i(\bar{r},t)\right), \quad i = 0,1,\ldots,b. \end{aligned} \quad (15)$$

However, the consistency of Eq. (15) with Eq. (5) needs to be mathematically justified. A_1, A_2, and A_3 are arbitrary constants imposed in Eqs. (14) and (15) and are derived subsequently in the further sections. Though written discretely for the ith PDF, Eq. (15) is not an algebraic difference equation. Approximation of derivatives is solicited to initiate the computations. We further provide the finite difference discretization(s) of Eq. (15) as follows:

For $i = 0$, i.e., particle distribution functions that are stationary at the center of the lattices, discretization of spatial

derivatives are performed by the second order central difference scheme, as follows:

$$\text{term II} \approx A_2\left(\frac{1}{r}\right)\left(\frac{\Delta t}{\Delta r}\right)\left(\frac{T(r+\Delta r,t)-T(r-\Delta r,t)}{2}\right)_{i=0}, \tag{16a}$$

$$\text{term III} \approx A_3\left(\frac{1}{r}\right)\left(\frac{\Delta t}{\Delta r}\right)\left(\frac{f_0(r+\Delta r,t)-f_0(r-\Delta r,t)}{2}\right). \tag{16b}$$

For $i \neq 0$, i.e., particle distribution functions that are moving consecutively with nonzero velocity, discretization is performed by first order upwind scheme as follows:

$$\text{term II} \approx A_2\left(\frac{1}{r}\right)\left[\left[\left[\frac{1}{\bar{e}_i},0\right]\right]\{T(r,t)-T(r-\Delta r,t)\} + \left[\left[0,-\frac{1}{\bar{e}_i}\right]\right]\{T(r+\Delta r,t)-T(r,t)\}\right]_{i\neq 0}, \tag{17a}$$

$$\text{term III} \approx A_2\left(\frac{1}{r}\right)\left[\left[\left[\frac{1}{\bar{e}_i},0\right]\right]\{f_i(r,t)-f_i(r-\Delta r,t)\} + \left[\left[0,-\frac{1}{\bar{e}_i}\right]\right]\{f_i(r+\Delta r,t)-f_i(r,t)\}\right]_{i\neq 0}, \tag{17b}$$

where $\bar{e}_i$ is the velocity given by

$$\bar{e}_i = \begin{cases} \frac{\Delta r}{\Delta t} & i = 1,3,5\ldots \\ -\frac{\Delta r}{\Delta t} & i = 2,4,6\ldots \end{cases}. \tag{17c}$$

In Eqs. (17a) and (17b), $[\![A,B]\!]$ is an operator denoting the greater of A and B [50]. Each PDF $f_i(\bar{r},t)$ is located in the center of the ith lattice. For a given time step, the energy transport is obtained following two steps: (i) when the particle distribution functions collide on each face of the lattice (collision step), followed by (ii) streaming of particle distribution functions towards the next lattice (streaming step). Instead of discretization, following previous investigations [29,30], term I in Eq. (15), i.e., $\frac{\partial T(\bar{r},t)}{\partial t}$, can be related to mesoscopic PDF $f_i(\bar{r},t)$ as follows:

$$\frac{\partial T(\bar{r},t)}{\partial t} = \frac{\sum_{i=0}^{b} f_i(\bar{r},t)}{\tau_q}. \tag{18}$$

In order to retrieve $\frac{\partial T(\bar{r},t)}{\partial t}$, we need to compute $f_i(\bar{r},t)$ following Eq. (15), where coefficients A_1, A_2, and A_3, source term $\varphi(\bar{r},t)$, and lastly equilibrium PDF $f_i^{(0)}$ stand unknown. We employ Chapman-Enskog multiscale expansion to derive theses unknowns and to further establish mathematical consistency between LBM and DPL formulation. PDFs f_i are expanded up to the second order with respect to the perturbation parameter $\varepsilon(|\varepsilon| \ll 1)$ as

$$f_i = f_i^{(0)} + \varepsilon f_i^{(1)} + \varepsilon^2 f_i^{(2)} + O(\varepsilon^3). \tag{19}$$

The summations of PDFs satisfy the following constraints:

$$\sum f_i = \sum f_i^{(0)} \quad \text{and} \quad \sum f_i^{(1)} = \sum f_i^{(2)} = 0. \tag{20}$$

Scaling of time and space are performed as follows:

$$\partial_t = \varepsilon \partial_{t^{(1)}} + \varepsilon^2 \partial_{t^{(2)}} + O(\varepsilon^3), \tag{21}$$

$$\partial_r = \varepsilon \partial_{r^{(1)}} + O(\varepsilon^2), \tag{22}$$

$$\frac{1}{r} = \varepsilon \frac{1}{r^{(1)}}. \tag{23}$$

The temporal (unsteady) term $\frac{\partial T}{\partial t}$ and laser irradiation term φ in Eq. (15) are assumed to be of the scale of (ε^2) as [49]

$$\frac{\partial T}{\partial t} = \varepsilon^2 \frac{\partial T}{\partial t^{(2)}}, \tag{24}$$

$$\varphi_i = \varepsilon^2 \varphi_i^{(2)}. \tag{25}$$

In Eq. (15), the expansion of $f_i(\bar{r},\bar{e}_i\Delta t, t+\Delta t)$ around PDF $f_i(\bar{r},t)$ by Taylor's series is accomplished first. As per the perturbation expansion in Eq. (19), $f_i(\bar{r},t)$ is further expanded around equilibrium PDF $f_i^{(0)}$. Considering the above expansions and implementing the scaling operations performed in Eqs. (21)–(25) the resulting equations of the order of ε, ε^2 are obtained from Eq. (15) respectively as

$$\partial_{t^{(1)}} f_i^{(0)} + \partial_{r_\alpha^{(1)}} e_{i\alpha} f_i^{(0)} = -\frac{1}{\tau} f_i^{(1)}, \tag{26}$$

$$\partial_{t^{(2)}} f_i^{(0)} + \left(-\tau + \frac{\Delta t}{2}\right)\left(\partial_{t^{(1)}} + \partial_{r_\alpha^{(1)}} e_{i\alpha}\right)^2 f_i^{(0)} = -\frac{1}{\tau} f_i^{(2)} + A_1 \frac{\partial T}{\partial t_{(2)}} + \frac{1}{r^{(1)}} \partial_{r_\alpha^{(1)}}\left(A_2 T + A_3 f_i^{(0)}\right) + \varphi_i^{(2)}. \tag{27}$$

Summing, Eqs. (26) and (27) from $i = 0$ to b results in

$$\tau_q \partial_{t^{(1)}} \frac{\partial T}{\partial t} + \partial_{r_\alpha^{(1)}} \sum_{i=0}^{b} e_{i\alpha} f_i^{(0)} = -\frac{1}{\tau} \sum_{i=0}^{b} f_i^{(1)}, \tag{28}$$

$$\partial_{t^{(2)}} \sum_{i=0}^{b} f_i^{(0)} + \left(-\tau + \frac{\Delta t}{2}\right)\left(\tau_q \partial_{t^{(1)}}^2 \frac{\partial T}{\partial t} + \partial_{r_\alpha^{(1)}} \partial_{r_\beta^{(1)}} \sum_{i=0}^{b} e_{i\alpha} e_{i\beta} f_i^{(0)} + 2\partial_{t^{(1)}} \partial_{r_\alpha^{(1)}} \sum_{i=0}^{b} e_{i\alpha} f_i^{(0)}\right) = -\frac{1}{\tau} \sum_{i=0}^{b} f_i^{(2)} A_1 (b+1) \frac{\partial T}{\partial t_{(2)}} + \frac{1}{r^{(1)}} \partial_{r_\alpha^{(1)}} \left[A_2 T (b+1) + A_3 \tau_q \frac{\partial T}{\partial t}\right] + (b+1)\varphi_i^{(2)}. \tag{29}$$

With the operation, Eq. (26)$\times\varepsilon$+ Eq. (27)$\times\varepsilon^2$ performed and the following constraints are imposed:

$$\sum_{i=0}^{b} e_{i\alpha} f_i^{(0)} = 0, \tag{30}$$

$$\sum_{i=0}^{b} e_{i\alpha} e_{i\beta} f_i^{(0)} = \lambda T + \tau_T \gamma \frac{\partial T}{\partial t}. \tag{31}$$

In terms of temperature, the following temperature equation is obtained from Eq. (29):

$$\begin{aligned}
&\tau_q \frac{\partial^2 T}{\partial t^2} - A_1(b+1)\frac{\partial T}{\partial t} \\
&= \left(\tau - \frac{\Delta t}{2}\right)\left[\lambda \frac{\partial^2 T}{\partial r^2} + \tau_T \gamma \frac{\partial^3 T}{\partial r^2 \partial T}\right] \\
&\quad + \frac{1}{r}\left[A_2(b+1)\frac{\partial T}{\partial r} + A_3 \tau_q \frac{\partial^2 T}{\partial r \partial T}\right] + (b+1)\varphi \\
&\quad + \left(\tau - \frac{\Delta t}{2}\right)\varepsilon^2 \partial_{t_{(1)}} \partial_{t_{(1)}} \left(\tau_q \frac{\partial T}{\partial t} + O(\varepsilon^3) + O(\Delta t^3)\right).
\end{aligned} \tag{32}$$

In Eqs. (31) and (32), λ, γ are arbitrary constants (unknown). Since Eq. (32) needs to be consistent with the actual DPL governing energy equation [Eq. (5)], all the related coefficients, arbitrary constants $(A_1, A_2, A_3, \lambda, \gamma)$, and dimensional source term (φ) imposed in the formulation are derived by comparing Eq. (32) with Eq. (5) as follows:

$$A_2 = -\left(\frac{1}{b+1}\right), \quad A_2 = \left(\frac{2\alpha}{b+1}\right), \quad A_3 = \left(2\alpha \frac{\tau_T}{\tau_q}\right), \tag{33a}$$

$$\lambda = \frac{\alpha}{(\tau - \Delta t/2)}, \quad \gamma = \frac{\alpha}{(\tau - \Delta t/2)}, \tag{33b}$$

$$\varphi_i = \frac{G(r,t)}{b+1}, \tag{33c}$$

where $\alpha = (\frac{k}{\rho c})$ is the thermal diffusivity of the GNS. The truncation error term in this LBM scheme can be expressed as follows:

$$T_E = \left(\tau - \frac{\Delta t}{2}\right)\varepsilon^2 \partial_{t_{(1)}} \partial_{t_{(1)}} \left(\tau_q \frac{\partial T}{\partial t}\right) + O(\varepsilon^3) + O(\Delta t^3). \tag{34}$$

Now, for the one-dimensional spherical coordinate geometry, considering the D1Q3 lattice (i.e., substituting $b = 2$), the three equilibrium PDFs $f_o^{(0)}$, $f_1^{(0)}$, and $f_2^{(0)}$ are derived as follows:

$$f_1^{(0)} = f_2^{(0)} = \frac{\lambda}{2e^2} T + \frac{\tau_T \gamma}{2e^2} \frac{\partial T}{\partial t}, \tag{35a}$$

$$f_0^{(0)} = \tau_q \frac{\partial T}{\partial t} - \frac{\lambda}{e^2} T - \frac{\tau_T \gamma}{e^2} \frac{\partial T}{\partial t}. \tag{35b}$$

With the discretization applied in Eqs. (16a) and (16b) and in Eqs. (17a) and (17b), coefficients $A_1, A_2, A_3, \lambda, \gamma$, source term φ derived in Eqs. (33a)–(33c), and finally equilibrium PDFs $f_o^{(0)}$, $f_1^{(0)}$, and $f_2^{(0)}$ obtained in Eqs. (35a) and (35b), solution of Eq. (15), i.e., $f_i(\bar{r},t)$ distributions, can be computed thoroughly. With the known $f_i(\bar{r},t)$ distributions, we retrieve $\frac{\partial T(\bar{r},t)}{\partial t}$ and temperature at an advance time level $(t + \Delta t)$ is obtained from the Taylor series expansion up to the second order accuracy,

$$\begin{aligned}
&T(\bar{r}, t + \Delta t) \\
&= T(\bar{r},t) + \Delta t \frac{\partial T(\bar{r},t)}{\partial t} + \frac{\Delta t^2}{2} \frac{\partial^2 T(\bar{r},t)}{\partial t^2} + O(\Delta t^3).
\end{aligned} \tag{36}$$

Computations are initiated with the calculation of equilibrium PDF, $f_i^{(0)}(\bar{r},t)$ from the initial conditions depicted in Eq. (6a). The boundary conditions [Eq. (6b)] towards the solution are required in terms of PDF. Since at the center $(r = 0)$ and surface $(r = L)$ adiabaticlike boundary conditions prevail, following previous studies [29,30,48], we assume the PDFs are completely reflected from boundaries at any given instant of time signifying $f_1 = f_2$ at $r = 0$ and $f_2 = f_1$ at $r = L$. The schematic of D1Q3 lattice with implementation of boundary conditions is depicted in Fig. 3.

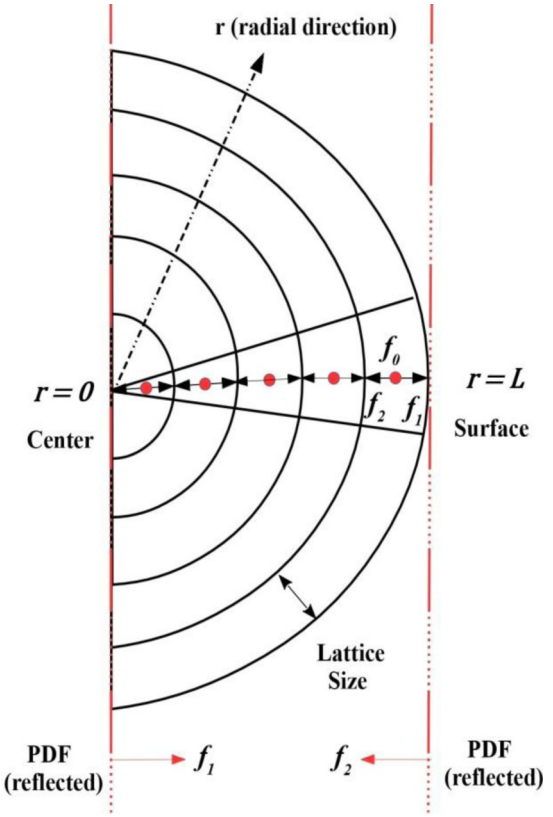

FIG. 3. Schematic of D1Q3 lattice of LBM formulation for concentric spherical coordinate geometry with implementation of boundary conditions.

B. Finite different method scheme (FDM1)

This three-level, implicit, unconditionally stable finite difference scheme proposed by McDonough *et al.* [31] was further extended by Mishra *et al.* [29] to solve the DPL governing equation in a cylindrical or spherical coordinate system without considering the volumetric source term. This

finite difference scheme inherits first order global accuracy and second order local accuracy in time. The detailed formulation and is provided in the Appendix A1, for reference. With required discretization(s) performed, for $N+1$ grid points, the following difference equations are obtained:

$$a_{1i}T_i^{m+1} + a_{2i}T_{i+1}^{m+1} + a_{3i}T_{i-1}^{m+1} = a_{4i}T_i^m + a_{5i}T_{i+1}^m + a_{6i}T_{i-1}^m + a_{7i}T_i^{m-1} + a_{8i}, \quad 1 \leqslant i \leqslant N-1, \tag{37}$$

where the, coefficients $a_{1i}, a_{2i}, \ldots a_{8i}$ are given by the following:

$$a_{1i} = \frac{\rho c \tau_q}{\Delta t} + \rho c + \frac{2k\tau_T}{(\Delta r)^2} + \frac{k\Delta t}{(\Delta r)^2}, \tag{38a}$$

$$a_{2i} = -\frac{k\tau_T}{(\Delta r)^2} - \frac{2k\tau_T}{2r_i\Delta r} - \frac{k\Delta t}{2(\Delta r)^2} - \frac{2k\Delta t}{4r_i\Delta r}, \tag{38b}$$

$$a_{3i} = -\frac{k\tau_T}{(\Delta r)^2} + \frac{2k\tau_T}{2r_i\Delta r} - \frac{k\Delta t}{2(\Delta r)^2} + \frac{2k\Delta t}{4r_i\Delta r}, \tag{38c}$$

$$a_{4i} = \frac{2\rho c \tau_q}{\Delta t} + \rho c + \frac{2k\tau_T}{(\Delta r)^2} - \frac{k\Delta t}{2(\Delta r)^2}, \tag{38d}$$

$$a_{5i} = -\frac{k\tau_T}{(\Delta r)^2} - \frac{2k\tau_T}{2r_i\Delta r} + \frac{k\Delta t}{2(\Delta r)^2} + \frac{2k\Delta t}{4r_i\Delta r}, \tag{38e}$$

$$a_{6i} = -\frac{k\tau_T}{(\Delta r)^2} + \frac{2k\tau_T}{2r_i\Delta r} + \frac{k\Delta t}{2(\Delta r)^2} - \frac{2k\Delta t}{4r_i\Delta r}, \tag{38f}$$

$$a_{7i} = -\frac{\rho c \tau_q}{\Delta t}, \tag{38g}$$

$$a_{8i} = G_i^m \Delta t = \left(g_i^m + \left(\frac{\partial g}{\partial t}\right)_i^m\right)\Delta t. \tag{38h}$$

C. Finite difference method (FDM2)

Here we provide an alternative discretization approach where, locally and globally second order accuracy is preserved in both time and space. The detailed formulation is provided in the Appendix A2, for reference. The reported three-level, implicit finite scheme leads to the following difference equations:

$$a_{1i}T_i^{m+1} + a_{2i}T_{i+1}^{m+1} + a_{3i}T_{i-1}^{m+1} = a_{4i}T_i^m + a_{5i}T_{i+1}^m + a_{6i}T_{i-1}^m + a_{7i}T_i^{m-1} + a_{8i}T_{i+1}^{m-1} + a_{9i}T_{i-1}^m + a_{10i}, \quad 1 \leqslant i \leqslant N-1, \tag{39}$$

where the coefficients $a_{1i}, a_{2i}, \ldots a_{10i}$ are derived as follows:

$$a_{1i} = \frac{\rho c}{2} + \frac{\rho c \tau_q}{\Delta t} + \frac{k\tau_T}{\Delta r^2} + \frac{k\Delta t}{2\Delta r^2}, \tag{40a}$$

$$a_{2i} = -\frac{k\tau_T}{2\Delta r^2} - \frac{k\tau_T}{2r_i\Delta r} - \frac{k\Delta t}{4\Delta r^2} - \frac{k\Delta t}{4r_i\Delta r}, \tag{40b}$$

$$a_{3i} = -\frac{k\tau_T}{2\Delta r^2} + \frac{k\tau_T}{2r_i\Delta r} - \frac{k\Delta t}{4\Delta r^2} + \frac{k\Delta t}{4r_i\Delta r}, \tag{40c}$$

$$a_{4i} = \frac{2\rho c \tau_q}{\Delta t} - \frac{k\Delta t}{\Delta r^2}, \tag{40d}$$

$$a_{5i} = \frac{k\Delta t}{2\Delta r^2} + \frac{k\tau_T}{2r_i\Delta r}, \tag{40e}$$

$$a_{6i} = \frac{k\Delta t}{2\Delta r^2} - \frac{k\tau_T}{2r_i\Delta r}, \tag{40f}$$

$$a_{7i} = \frac{\rho c}{2} - \frac{\rho c \tau_q}{\Delta t} + \frac{k\tau_T}{\Delta r^2} - \frac{k\Delta t}{2\Delta r^2}, \tag{40g}$$

$$a_{8i} = -\frac{k\tau_T}{2\Delta r^2} - \frac{k\tau_T}{2r_i\Delta r} + \frac{k\Delta t}{4\Delta r^2} + \frac{k\Delta t}{4r_i\Delta r}, \tag{40h}$$

$$a_{9i} = -\frac{k\tau_T}{2\Delta r^2} + \frac{k\tau_T}{2r_i\Delta r} + \frac{k\Delta t}{4\Delta r^2} - \frac{k\Delta t}{4r_i\Delta r}, \tag{40i}$$

$$a_{10i} = G_i^m \Delta t = \left(g_i^m + \left(\frac{\partial g}{\partial t}\right)_i^m\right)\Delta t. \tag{40j}$$

D. Finite difference method (FDM3) [15]

In order to assess the accuracy of the present results based on the formulation presented above, the same problem is also revisited and further validated against the formulation proposed in the literature by Dai *et al.* [15,28]. For completeness, the scheme is briefly presented below. Time and space discretizations lead to the following difference equations:

$$a_{1i}T_i^{m+1} + a_{2i}T_{i+1}^{m+1} + a_{3i}T_{i-1}^{m+1} = a_{4i}T_i^m + a_{5i}T_{i+1}^m + a_{6i}T_{i-1}^m + a_{7i}T_i^{m-1} + a_{8i}T_{i+1}^{m-1} + a_{9i}T_{i-1}^m + a_{10i}, \quad 1 \leqslant i \leqslant N-1, \tag{41}$$

where the coefficients $a_{1i}, a_{2i}, \ldots a_{10i}$ are derived as follows:

$$a_{1i} = \frac{2\rho c \tau_q}{\Delta t} + \rho c + \frac{r_{i+\frac{1}{2}}^2 k}{r_i^2(\Delta r)^2}\left(\frac{\Delta t}{2} + \tau_T\right) + \frac{r_{i-\frac{1}{2}}^2 k}{r_i^2(\Delta r)^2}\left(\frac{\Delta t}{2} + \tau_T\right), \tag{42a}$$

$$a_{2i} = -\frac{r_{i+\frac{1}{2}}^2 k}{r_i^2(\Delta r)^2}\left(\frac{\Delta t}{2} + \tau_T\right), \tag{42b}$$

$$a_{3i} = \frac{r_{i-\frac{1}{2}}^2 k}{r_i^2(\Delta r)^2}\left(\frac{\Delta t}{2} + \tau_T\right), \tag{42c}$$

$$a_{4i} = \frac{2\rho c \tau_q}{\Delta t} - \frac{r_{i+\frac{1}{2}}^2 k\Delta t}{r_i^2(\Delta r)^2} - \frac{r_{i-\frac{1}{2}}^2 k\Delta t}{r_i^2(\Delta r)^2}, \tag{42d}$$

$$a_{5i} = \frac{r_{i+\frac{1}{2}}^2 k\Delta t}{r_i^2(\Delta r)^2}, \tag{42e}$$

$$a_{6i} = \frac{r_{i-\frac{1}{2}}^2 k\Delta t}{r_i^2(\Delta r)^2}, \tag{42f}$$

$$a_{7i} = \frac{r_{i+\frac{1}{2}}^2 k}{r_i^2(\Delta r)^2}\left(\frac{\Delta t}{2} - \tau_T\right), \tag{42g}$$

$$a_{8i} = \rho c - \frac{2\rho c \tau_q}{\Delta t} + \frac{r_{i+\frac{1}{2}}^2 k}{r_i^2(\Delta r)^2}\left(\tau_T - \frac{\Delta t}{2}\right) + \frac{r_{i-\frac{1}{2}}^2 k}{r_i^2(\Delta r)^2}\left(\tau_T - \frac{\Delta t}{2}\right), \tag{42h}$$

$$a_{9i} = \frac{r_{i-\frac{1}{2}}^2 k}{r_i^2 (\Delta r)^2}\left(\frac{\Delta t}{2} - \tau_T\right), \tag{42i}$$

$$a_{10i} = G_i^m \Delta t = \left(g_i^m + \left(\frac{\partial g}{\partial t}\right)_i^m\right)\Delta t. \tag{42j}$$

It can be observed that the difference equations in Eqs. (37), (39), and (41) have three time levels, viz., $m-1$, m, and $m+1$, where the right-hand side contains the known values at time levels $m-1$ and m. In order to solve these equations, discretization of initial conditions and boundary conditions are solicited. We apply forward difference discretization of the initial condition (time derivative term) [Eq. (6b)] and the forward for space derivative at $r = 0$ and the backward difference for space derivative at $r = L$ of boundary conditions [Eq. (6b)] result in

$$\text{initial condition: } T_i^1 = T_i^0, \tag{43a}$$

$$\text{boundary conditions: } T_1^m = T_0^m, \quad T_{N-1}^m = T_N^m. \tag{43b}$$

Hence the present algebraic (difference) equations, obtained from finite difference schemes FDM1 [Eq. (37)], FDM2 [Eq. (39)], and FDM3 [Eq. (41)] with discretized initial and boundary conditions presented in Eqs. (43a) and (43b), form a system of linear equation(s) with a tridiagonal coefficient matrix. Because of being extremely efficient [50], all the $N+1$ linear algebraic equations have been solved using the tridiagonal matrix algorithm (Thomas algorithm). The steady-state (SS) condition was ascertained when the root mean average of the square of the differences of temperatures at two consecutive time levels, at all discrete i locations was $\leqslant$ the set limit as per the L_2 norm, as follows:

$$\xi_2 = \sqrt{\frac{\sum_{i=0}^{N}\left(T_i^m - T_i^{m-1}\right)^2}{(N+1)}}. \tag{44}$$

E. Heat flux distribution and net entropy production rate

With temporal temperature distribution retrieved by the above numerical schemes, the nature of the heat flux distribution can also be obtained by discretization of Eq. (3) by a second order central difference scheme. Physical interpretation of generalized absolute temperature from the SPL or DPL framework(s) is investigated by studying the net entropy production rate under equilibrium and nonequilibrium (if required) situations by classical and extended irreversible thermodynamics respectively. Formulations of net entropy production rate characteristics are illustrated as follows.

Based on the framework of classical irreversible thermodynamics (CIT), following the postulates of local thermodynamic equilibrium (LTE), the entropy of a small part of the system of specific volume v and specific internal energy u during nonequilibrium transitions (e.g., spontaneous transfer of heat from higher to lower temperature) can be defined under local thermodynamic equilibrium as

$$s = s(u,v). \tag{45}$$

The definition of equilibrium absolute temperature θ can be extended from property relations as the partial derivative of s with respect to u,

$$\frac{1}{\theta} = \left(\frac{\partial s(u,v)}{\partial u}\right)_v. \tag{46}$$

Following the framework of the extended irreversible thermodynamics (EIT), thermodynamic properties are redefined suitably to inculcate the nonequilibrium attribute(s). For high-rate heat flux applications, generalized (nonequilibrium) entropy of a small part of the system of specific volume v and specific internal energy u is considered to be an additional function of the local heat flux q and is defined as follows [38–40]:

$$s = s(u,v,q). \tag{47}$$

Nonequilibrium absolute temperature Θ can be interpreted as

$$\frac{1}{\Theta} = \left(\frac{\partial s(u,v,q)}{\partial u}\right)_{(v,q)}. \tag{48}$$

Nonequilibrium entropy and equilibrium entropy can be mathematically bridged up by expansion of $s(u,v,q)$ about $s(u,v)$ up to second order approximation in q as follows [40]:

$$s(u,v,q) = s(u,v) - \underbrace{\frac{\Im}{2}(q\cdot q)}_{\mathrm{I}}. \tag{49}$$

$\Im$ is the expansion parameter in Eq. (49) and will be interpreted subsequently. Equilibrium entropy $s(u,v)$ and nonequilibrium entropy $s(u,v,q)$ differ because of the presence of term I in the right-hand side of Eq. (49). For applications involving a lower rate of heat flux ($q \ll 1$ W/m^2) transport, a magnitude of $(q\cdot q)$ on term I of Eq. (49) becomes negligibly small. In this context, $s(u,v,q)$ is reduced to the equilibrium entropy $s(u,v)$ and Θ becomes equivalent to θ. However for high-rate laser irradiation applications, $s(u,v)$ and $s(u,v,q)$ differ. Differentiation of Eq. (49) partially with respect to u and substituting expressions of Eqs. (46) and (48) into Eq. (49) further leads to the relation between θ and Θ,

$$\frac{1}{\Theta} = \left(\frac{1}{\theta} - \frac{1}{2}\left(\frac{\partial \Im}{\partial u}\right)_{(v,q)}(q\cdot q)\right). \tag{50}$$

Considering the GNS to be incompressible, a differential form of $s(u,v,q)$ can be expressed as

$$\begin{aligned} ds(u,v,q) &= ds(u,q) \\ &= \left(\frac{\partial s}{\partial u}\right)_q du + \left(\frac{\partial s}{\partial q}\right)_u dq \\ &= \left(\frac{du}{\Theta} - \Im q\cdot dq\right) \end{aligned} \tag{51}$$

Equation (51) can be further rewritten in temporal term(s) as follows:

$$\frac{\partial s(u,v,q)}{\partial t} = \left\{\frac{1}{\Theta}\left(\frac{\partial u}{\partial t}\right) - \Im q\cdot\frac{\partial q}{\partial t}\right\}. \tag{51a}$$

If absolute temperature history T, retrieved under the SPL or DPL framework, is generalized to nonequilibrium absolute temperature Θ, then further substitution of the expression of

$\frac{\partial u}{\partial t}$ from Eq. (2) into Eq. (51a) yields

$$\frac{\partial s(u,v,q)}{\partial t} = \left(-\frac{\nabla\cdot q}{\rho\,\Theta} + \frac{g}{\rho\,\Theta} - \Im q\cdot\frac{\partial q}{\partial t}\right). \tag{52}$$

Substituting the identity relation $\nabla\cdot(\frac{q}{\Theta}) = (\frac{\nabla\cdot q}{\Theta} - \frac{q\cdot\nabla\Theta}{\Theta^2})$ into Eq. (52) eventually results in the generalized entropy transfer equation (with nonequilibrium terms)

$$\underbrace{\left[\rho\frac{\partial s(u,v,q)}{\partial t} + \nabla\cdot\left(\frac{q}{\Theta}\right)\right]}_{\text{I}} = \left(\frac{g}{\Theta} - \frac{q\cdot\nabla T}{\Theta^2} - \underbrace{\rho\Im q\cdot\frac{\partial q}{\partial t}}_{\text{II}}\right) = S_{\text{gen}}. \tag{53}$$

Equation (53) can be further reduced to the equilibrium entropy transfer equation (Clausius-Duhem inequality) when the (1) term II of Eq. (53) does not appear and (2) absolute temperature history T is reduced to equilibrium absolute temperature θ as follows:

$$\left[\rho\frac{\partial s(u,v)}{\partial t} + \nabla\cdot\left(\frac{q}{\theta}\right)\right] = \left(\frac{g}{\theta} - \frac{q\cdot\nabla T}{\theta^2}\right) = S_{\text{gen}}. \tag{54}$$

If Eq. (54) results in negative equilibrium entropy production rate, $S_{\text{gen}} < 0$ (i.e., violation of the Clausius-Duhem inequality), Eq. (53) is subsequently employed to investigate the compatibility of the corresponding framework (SPL or DPL) with the second law of thermodynamics under the nonequilibrium (EIT) framework. In order to evolve q and ∇T and further derive $\Im$, we simply express the right-hand side of Eq. (53) as follows:

$$-\left(\frac{\nabla\Theta}{\Theta^2} + \rho\Im\frac{\partial q}{\partial t}\right) = \left(\chi q + \aleph\frac{\partial}{\partial t}(\nabla\Theta)\right), \tag{55}$$

where χ and $\aleph$ are arbitrary positive quantities (unknown). Equation (55) can be further rearranged as follows:

$$\left(q + \frac{\rho\Im}{\chi}\frac{\partial q}{\partial t}\right) = -\left(\frac{\nabla\Theta}{\chi\,\Theta^2} + \frac{\aleph}{\chi}\frac{\partial}{\partial t}(\nabla\Theta)\right). \tag{56}$$

Comparing the coefficients of Eq. (56) with the first order DPL equation, i.e., Eq. (3), yields

$$\frac{\rho\Im}{\chi} = \tau_q, \quad \frac{1}{\chi\Theta^2} = k, \quad \frac{\aleph}{\chi} = k\tau_T. \tag{57a}$$

Rearranging terms from the above relations in Eq. (57a); coefficients $\Im$, $\aleph$, and χ are derived as

$$\Im = \frac{\tau_q}{\rho k\Theta^2}, \quad \chi = \frac{1}{k\Theta^2}, \quad \aleph = \frac{\tau_T}{\Theta^2}. \tag{57b}$$

Inserting the magnitude of $\Im$ into Eq. (50) and further rearrangement leads to

$$\left(\frac{\theta-\Theta}{\theta}\right) = \frac{\tau_q}{\rho ck}\left(\frac{q\cdot q}{\Theta^2}\right). \tag{58}$$

Equation (58) illustrates the quantitative difference between equilibrium and nonequilibrium absolute temperature. Similarly, the final expression of the net nonequilibrium entropy production rate following the DPL governing equation can be derived by inserting the magnitude of $\Im$ into Eq. (53) as follows:

$$S_{\text{gen}} = \left\{\frac{g}{\Theta} - \frac{q}{\Theta^2}\cdot\left(\nabla\Theta + \frac{\tau_q}{k}\frac{\partial q}{\partial t}\right)\right\} = \left\{\frac{g}{\Theta} + \frac{q}{\Theta^2}\cdot\left(\frac{q}{k} + \tau_T\frac{\partial}{\partial t}(\nabla\Theta)\right)\right\}. \tag{59}$$

The above formulation [Eq. (59) is written under the DPL framework, which can be reduced to SPL and classical diffusion frameworks. However, Eq. (59) can be generalized to derive the equilibrium entropy production rate as

$$S_{\text{gen}} = \left(\frac{g}{\theta} - \frac{q\cdot\nabla\theta}{\theta^2}\right). \tag{60}$$

III. RESULTS AND DISCUSSION

In this section, the above illustrated numerical schemes are further employed to predict the temperature history of the GNS, irradiated with various short-pulse laser sources. In order to understand how the thermophysical response of the single-phase lag (SPL) and dual-phase lag (DPL) frameworks (with various lag ratios) differs and to further characterize thermophysical anomalies (if any), heat flux distribution and entropy generation characteristics are studied under the equilibrium and nonequilibrium paradigm. An expression of effective thermal conductivity is formulated considering unsteady and size (radius) effects, and the temporal thermophysical response is illustrated. The computational performance of each numerical scheme is also highlighted.

A. Validation, accuracy, and grid convergence test

Before proceeding to discuss all the results in hand in greater detail, the accuracy and grid convergence test of the above reported schemes are provided. Let us first consider the following function:

$$T_{ex}(r,t) = e^{(-\pi^2 t)}\cos(\pi r). \tag{61}$$

$T_{ex}(r,t)$ is globally continuous and derivable with respect to r and t and subsequently satisfies the following DPL-like partial differential equation:

$$\frac{\partial T}{\partial T} + \left(\frac{1}{2\pi^2}\right)\frac{\partial^2 T}{\partial t^2} = \frac{1}{r^2}\frac{\partial}{\partial r}\left(r^2\frac{\partial T}{\partial r}\right) + \frac{1}{\pi^2 r^2}\frac{\partial}{\partial r}\left(r^2\frac{\partial^2 T}{\partial t\partial r}\right) - \frac{\pi^2}{2}e^{(-\pi^2 t)}\cos(\pi r); \quad 0\leqslant r\leqslant 1. \tag{62}$$

Therefore Eq. (61) can be considered an analytical solution of Eq. (62) [15]. Since mathematically Eq. (62) appears to be equivalent to the initial boundary value problem describing the DPL governing equation for spherical coordinate geometry (with a spatially temporally varying source term), the validation and accuracy of numerical methods (depicted in Sec. II) can be assessed by employing them to solve Eq. (62) and subsequently compare with the analytical solution, $T_{ex}(r,t)$. For any given instant t, the relative error is calculated as per the L_1 norm as follows:

$$\xi_1 = \frac{\sum_{i=0}^{N}|T_i - T_{ex}|}{(N+1)}. \tag{63}$$

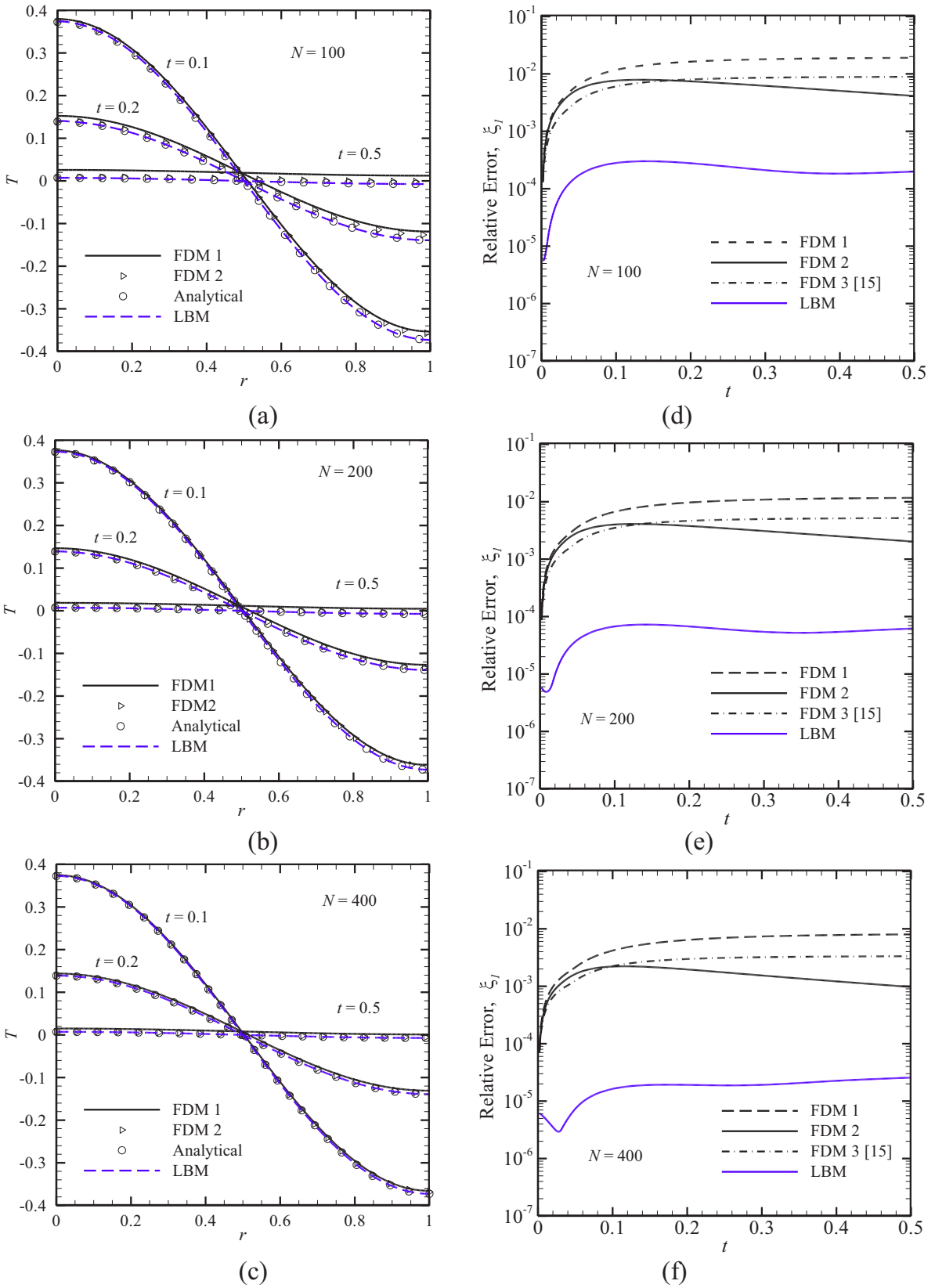

FIG. 4. (a)–(c) Distribution of T vs r at $t = 0.1$, 0.2, and 0.5 and (d)–(f) relative error, ξ_1 vs t plot for $N = 100$, $N = 200$, and $N = 400$.

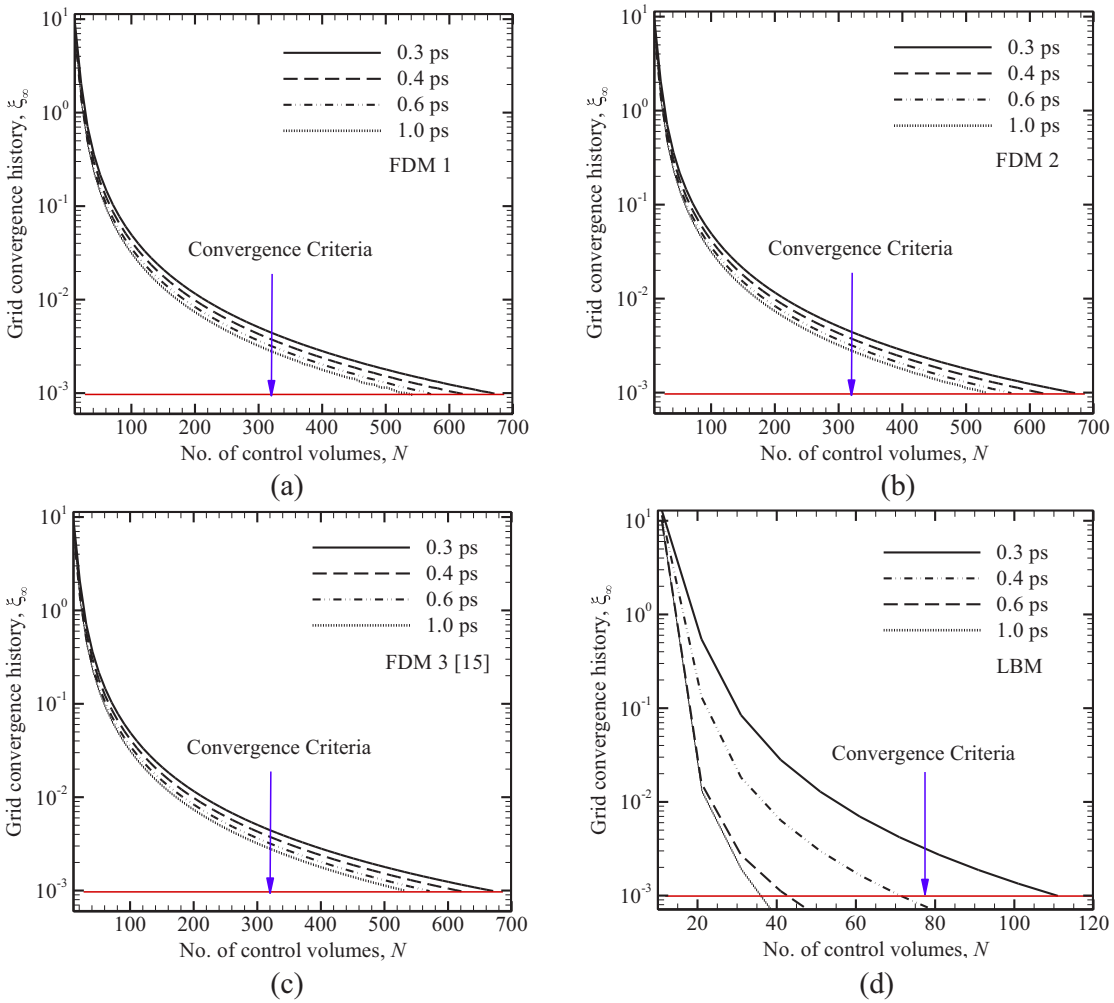

FIG. 5. Grid convergence history ($\xi_\infty \leqslant 10^{-3}$) for (a) FDM1, (b) FDM2, (c) FDM3 [15], and (d) LBM with numbers of lattice or control volumes.

In Eq. (63), T_i and T_{ex} are the results at the ith ($0 \leqslant i \leqslant N$) grid from the numerical scheme(s) and analytical method respectively. A lesser magnitude of ξ_1 at any given temporal instants of t and r signify an accurate result that approaches the analytical solution. A detailed description of numerical solution by all the schemes at $t = 0.1$, 0.3, and 0.5 along with an analytical solution [presented in Eq. (61)] for various numbers of grid points ($N = 100$, 200, and 400) are elucidated in Figs. 4(a)–4(c). Distribution of the relative error ξ_1 with t for all the numerical schemes are further presented in Figs. 4(d)–4(f).

In terms of accuracy (i.e., least magnitude of relative error), the LBM scheme is observed to be superior to other numerical schemes, for all situations. With the exception of the temporal region $t \leqslant 0.15$, accuracy of the FDM2 scheme is found to be higher than FDM3 [15]. FDM1 [29–31] yields the least accuracy among all the schemes in all situations although the accuracy of this scheme can be appreciably enhanced with increasing grid points. For $N = 400$, the accuracy of FDM1 is found to retain less than 10^{-2} for all values of t. A similar trend is observed for other numerical schemes too, when the number of grid points is increased. For $N = 400$, the LBM scheme reports the highest accuracy with $\xi_1 \leqslant 10^{-4}$, the least among all the numerical schemes for all values of t.

Following the lead by several researchers [15,17,28,43], in order to solve the dimensional DPL governing energy equation, the averaged thermophysical properties of gold are considered to be $\rho = 19\,300$ (kg/m^3), $c = 129$ (J/kg K), $\tau_q = 8.5$ ps, and $\tau_T = 90.0$ ps. In Secs. III A–III E, the usual bulk thermal conductivity (k_b) at initial (room) temperature (300 K) is adopted to be the thermal conductivity, i.e., $k = k_b = 315$ (W/mK). However, temporal as well as size (radius) dependence of thermal conductivity and a detailed review of the corresponding thermophysical response is elucidated in Sec. III F. Before presenting all the results, the effect of grid sizing on temperature distribution is ascertained. For a 100-nm GNS, an additional simulation for various numbers of equispaced grids in multiples of 10 ($N = 10$, 20, 30, 40, and so on) is carried by considering the time step to be $\Delta t = 0.0001$ ps, unless required convergence ($\xi_\infty \leqslant 10^{-3}$) is obtained as per L_∞ norms, expressed as

$$\xi_\infty = \max_N |T_{N'} - T_N|, \tag{64}$$

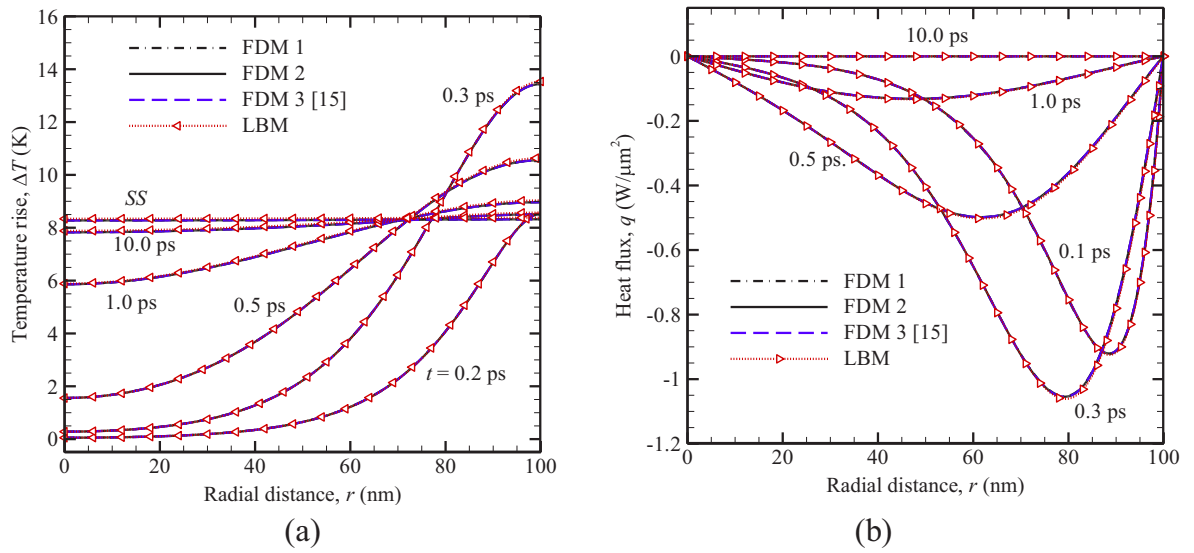

FIG. 6. Temporal temperature rise and heat flux distribution of a 100-nm GNS irradiated with one laser pulse under DPL framework by all the numerical schemes.

where N' and N represent the previous and current numbers of control volumes respectively in Eq. (64). Compared to the FDM schemes (FDM1, FDM2, and FDM3), the LBM scheme dramatically accelerates the decay of ξ_∞ with N and finally convergence is witnessed for much smaller numbers of grid points for all time instants under investigation. This will save a considerable amount of computational storage to obtain grid-independent results with reasonable accuracy by the LBM scheme. All the results at $t = (0.3 - 1.0)$ ps are depicted in Fig. 5 for all the numerical schemes till required convergence.

With the validation of numerical codes performed and the grid convergence test accomplished, numerical experiments are performed to obtain the characteristics of temporal temperature history and heat flux distribution, under DPL and SPL frameworks.

B. Temporal temperature rise and heat flux distribution by DPL and SPL frameworks

Under the DPL framework, temporal temperature rise ($\Delta T = T - T_0$) and heat flux [$q(r,t)$] distribution within the interior of a GNS of radius 100 nm, irradiated by a single laser pulse, are depicted in Fig. 6 by all the numerical schemes (FDM and LBM), till required convergence is met and steady state (SS) is subsequently highlighted.

Solutions obtained from all the schemes are observed to match exceedingly well with each other. Since the peak of a single laser pulse is situated at $2t_p = 0.20$ ps, the temperature of the GNS surface comprehensively increases (peaking time is 0.27 ps). From 0.3 ps onwards, the temperature of the interior is enhanced gradually leading to enlarged thermal penetration from surface to the interior of the GNS until steady state (SS) is witnessed. The gradual propagation (penetration) of heat flux

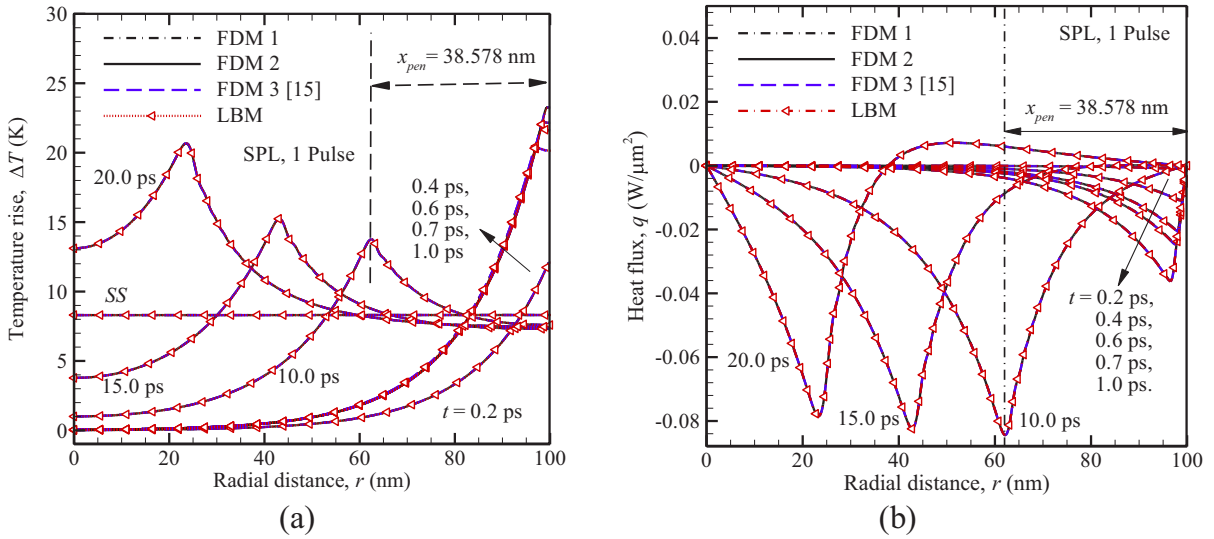

FIG. 7. Temporal temperature rise and heat flux distribution for a 100-nm GNS irradiated with one laser pulse under SPL framework by all the numerical schemes.

TABLE I. Penetration depth of thermal wave (x_{pen}) calculated from the surface of GNS at different transient levels.

Time, t(ps)	0.2	0.4	0.6	0.7	1.0	10.0	15.0	20.0	25.0
Penetration depth, x_{pen} (nm)	0.771	1.543	2.313	2.700	3.858	38.578	57.566	77.155	96.444

from surface to interior with time is also depicted in Fig. 6(b). This result is attributed to the consideration of an additional phase lag of temperature gradient (which is also defined as time required felicitating phonon-electron interactions) by the DPL framework that accounts for microscopic effects resulting in pronounced thermal response at the subpicosecond temporal scale.

As the interior of the GNS is thermally diffusive and the laser irradiation source term is temporally decaying, with the increase of time, the effect of thermal perturbation is found to be reduced. Temperature converges towards steady state (SS) and magnitude of heat flux distribution (approaching SS) is found to be negligibly small [Figs. 6(a) and 6(b)]. Results obtained from all the schemes match exceedingly well with each other. With the omission of τ_T, phonon-electron interaction is subsequently neglected and the DPL framework is reduced to the SPL framework. Being a special case of DPL ($\tau_T \to 0$), reliable temperature history under the SPL framework can be obtained by any of the described numerical schemes with reasonable accuracy. In order to understand the qualitative difference between DPL and SPL, the same problem is considered under the SPL framework in Fig. 7, where the temporal temperature rise and heat flux distribution is further elucidated.

Under the SPL framework, the temperature gradient is established instantaneously in the spatial domain while heat flux does not, leading to the experience of thermal inertia (τ_q) due to fast-transient heating and containment of collimated energy within the neighborhood of the GNS surface without effective transport towards the interior at the initial time of evaluation. Since the governing energy equation under the SPL framework is a second order wave equation which is hyperbolic in nature [characteristic thermal wave speed equal to $\sqrt{\frac{\alpha}{\tau_q}} = 3857.76$ m/s (for gold)]; this phenomenon of marginal thermal penetration can be explained in the light of thermal penetration depth, $x_{pen}(=\sqrt{\frac{\alpha}{\tau_q}}t)$ (measured from the surface towards the center) at any instant of time.

The penetration depth for thermal wave, measured from the surface of the GNS, at a given instant of time, for temporal level $t = (0.2-25.0)$ ps is further illustrated in Table I.

Up to $t = 0.6$ ps, it is observed that thermal penetration depth is lower than 2.5 nm from the surface of the GNS. This leads to negligible penetration of thermal energy towards the interior leading to further confinement of thermal energy within the neighborhood of the GNS surface. Therefore at the initial time of evaluation, the temperature rise of the GNS surface and the corresponding peaking time is observed to be larger compared to the DPL framework. The detailed prediction of maximum temperature rise at the GNS surface and corresponding peaking time by all the numerical schemes (LBM and FDM), for SPL, DPL, and classical diffusion frameworks is presented in Table II.

More clarity can be obtained by studying the normalized temperature change at the surface during the initial time of evaluation, presented in Fig. 8.

At the initial temporal domain ($t < t_{max}$), the temperature response of all the frameworks does not differ. However, the temporal region following peaking time shows a distinct thermal response of all the frameworks. Up to 2.0 ps, the SPL framework reports a maximum normalized temperature rise at the surface followed by classical diffusion and the DPL framework. However from $t = 3.0$ ps onward, a normalized temperature rise at the surface starts decreasing under the SPL framework. With a further rise of time, the normalized temperature predicted by the SPL framework attains the least magnitude, preceded by classical diffusion and the DPL framework respectively.

At a higher temporal range, transportation of localized energy is observed from the surface towards the interior, leading to enlargement of the thermal penetration depth. For, e.g., $t = 10.0$ ps, the thermal penetration depth (x_{pen}) is predicted to be 38.578 nm (cf. Table I), which matches well with the numerical solution depicted in Figs. 7(a) and 7(b). This region within the GNS, from surface to x_{pen}, is characterized by adverse temperature gradient ($\frac{\partial T}{\partial r} \leqslant 0$), since

TABLE II. Prediction of maximum temperature (ΔT_{max}) and the corresponding peaking time (t_{max}) at the 100-nm GNS surface irradiated with one laser pulse under the frameworks of DPL, SPL, and classical diffusion by all the numerical schemes.

Schemes:	LBM	FDM 1	FDM 2	FDM3 [15]
		DPL framework		
ΔT_{max}(K)	13.957	13.896	13.900	13.900
t_{max}(ps)	0.270	0.270	0.270	0.270
		SPL framework		
ΔT_{max}(K)	23.680	23.677	23.679	23.679
t_{max}(ps)	0.315	0.315	0.315	0.315
		Classical diffusion framework		
ΔT_{max}(K)		19.312		
t_{max}(ps)		0.290		

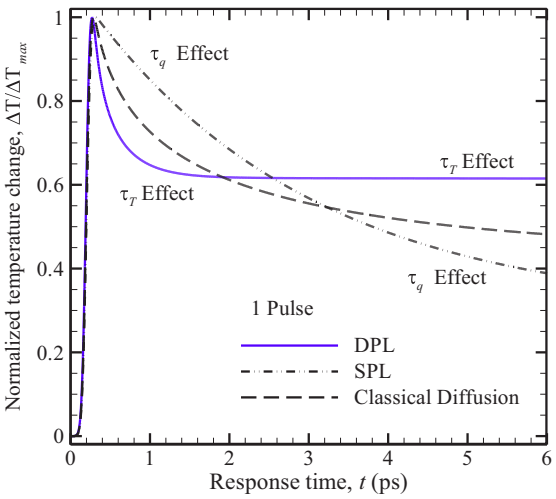

FIG. 8. Normalized temperature change at the surface of a 100-nm GNS irradiated with one laser pulse under the frameworks of DPL, SPL, and classical diffusion.

the temperature is found to overshoot (from the surface towards the interior). With the increase of time, as the discontinuity of the thermal wave moves further downstream with enhanced thermal penetration depth, the overshoot of temperature is found to be more severe. Further downstream from x_{pen}, a decay of temperature is witnessed on account of volumetric source term $G(r,t)$ alone, signifying a negligible amount of heat transported on account of conduction. Results retrieved by the DPL framework do not show this phenomenon of overshooting at all spatial and temporal domains. As discussed earlier, the paradox of overshooting from the point of view of the LTE hypothesis is well realized, since a higher temperature within the interior of the GNS does not support the feasibility of spontaneous transfer of heat from the surface (at lower temperature) to the interior (at higher temperature) as per the directional constraint imposed by the second law of thermody namics.

Surprisingly, instead of the presence of adverse temperature gradient, the domain prone to overshooting shows a nonpositive heat flux distribution [Fig. 7(b)], $q(r,t)$, in most of the temporal levels (0.2–15.0 ps). This observation signifies a transfer of heat from the surface to the interior of the GNS. Unlike Fourier's law of heat conduction, at a given instant of time, heat flux in the case of the SPL framework depends additionally on the rate of change of heat flux, $(\frac{\partial q}{\partial t})$. Following Eq. (3), it can be appreciated that on account of the simultaneous presence of negative heat flux distribution and adverse (negative) temperature gradient, the region of overshoot must mathematically satisfy $(\frac{\partial q}{\partial t}) \geqslant 0$. Therefore, the expected direction of heat transfer (surface to the interior) is retained for most of the subpicosecond temporal domain with some exceptions, obtained from 15 ps onwards. Since the laser-irradiation source is temporally decaying, the rate of change of heat flux starts decreasing with time and might lead to the change of sign of $(\frac{\partial q}{\partial t})$ to negative. Considering this circumstance, if the temperature gradient term of the SPL framework dominates over the term of temporal derivative of heat flux then, a non-negative heat flux distribution can be developed within the GNS (for, e.g., at $t = 20.0$ ps, positive heat flux distribution is witnessed within the domain of overshoot). As the adverse temperature gradient mostly reveals the right sense of heat flux distribution, unlike Fourier's law of heat conduction, the nature of heat flux distribution is difficult to assess singly from the temporal temperature history. In order to further verify and comment on the correctness of overshooting of temperature observed under the SPL framework described above, a detail thermodynamic analysis (entropy generation characteristics) remains the only recourse to provide the justified answer.

C. Entropy generation characteristics

First, the net (equilibrium) entropy production rate under the CIT framework is illustrated at various temporal instants. For $t = 0.4$ ps, the net entropy production rate under the DPL framework is observed to enhance from the surface to the interior following the trend of heat flux distribution [cf. Fig. 6(b)] and further to yield a positive definite entropy production rate everywhere [see Fig. 9(a)], whereas, at the same temporal instant (0.4 ps), under the SPL framework, a very thin thermal penetration depth leads to a marginal rise of the net entropy production rate. As thermal penetration depth enhances with the rise of time, from 0.7 ps onwards, appreciable temperature overshooting was observed under the SPL framework [Figs. 9(b)–9(f)]. This region of temperature overshoot (from surface to x_{pen}), for all instants of time $t = (1.0-20.0)$ ps, is observed to yield negative (equilibrium) entropy production rate. Local thermodynamic equilibrium no longer holds true and further, temperature overshooting observed under the SPL framework is characterized to be a highly nonlocal phenomenon. Therefore, the absolute temperature yielded by the SPL framework can no longer be interpreted as "(local) equilibrium temperature." With reference to the discontinuity of temperature and heat flux witnessed at a distance of x_{pen} from the surface of the GNS, at a given instant of time (Fig. 7), the entropy production rate (equilibrium) is further observed to discontinue at the same location. For, e.g., at $t = 15.0$ ps, the discontinuity of the entropy production rate is predicted to be 57.866 nm which matches accurately with the thermal penetration depth (cf. Table I). Further downstream from x_{pen} towards the center of the GNS, the rise of the entropy production rate is witnessed and subsequently yields a positive definite for all the time instants studied. The reason can be the presence of the volumetric source term (absorbed by the thermally participating GNS) on account of laser irradiation, since the effect of heat transfer on account of SPL conduction past x_{pen} is imperceptible.

Under the DPL framework, effective transportation and substantial penetration of thermal energy at an earlier time level, $t = (0.2 - 1.0)$ ps (compared to SPL framework), lead to the development of a small magnitude of temperature gradient and a marginal rise of entropy production rate (equilibrium) for 10.0 ps. and onwards. In order to investigate the thermodynamic consistency of the temperature overshooting observed from the SPL framework, the net entropy production rate is estimated considering nonequilibrium (nonlocal) high-rate heating effects, under the EIT framework. Results, however, reveal a positive definite (nonequilibrium) entropy production

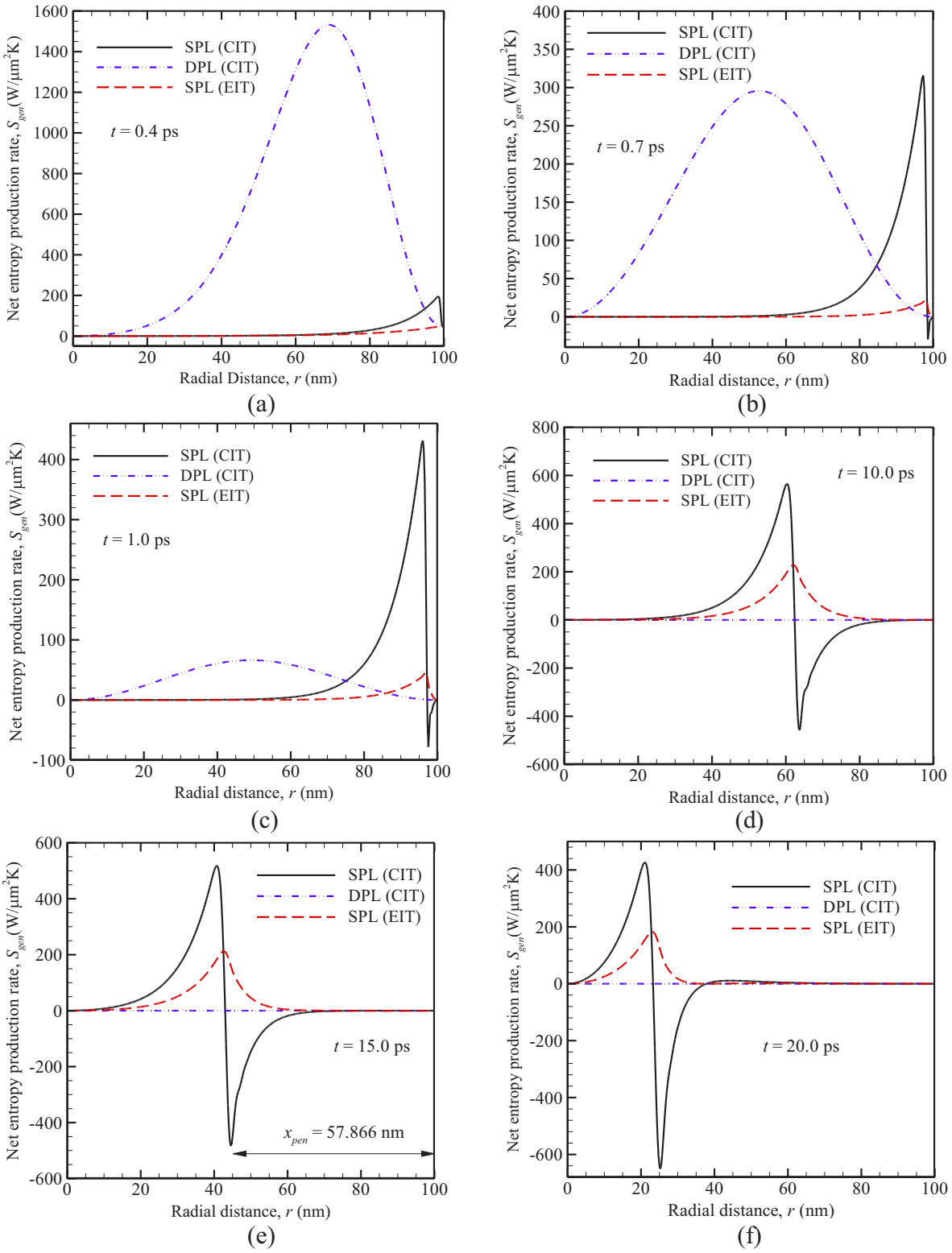

FIG. 9. Net entropy production rate distribution in 100-nm GNS irradiated with one laser pulse under DPL and SPL frameworks at (a) 0.4, (b) 0.7, (c) 1.0, (d) 10.0, (e) 15.0, (f) 20.0 ps.

rate, observed to increase from surface to x_{pen} (see Fig. 9). This result thermophysically connects the phenomenon of overshooting with extended irreversible thermodynamics. The absolute temperature history retrieved from the SPL framework can be qualitatively conceived to be a nonequilibrium temperature (or a nonlocal thermal disturbance). Unlike a (local) equilibrium temperature, any macroscopic interpretation of nonlocal thermal response as potential of heat flux (transferred through successive thermodynamic quasiequilibrium states) stands inappropriate.

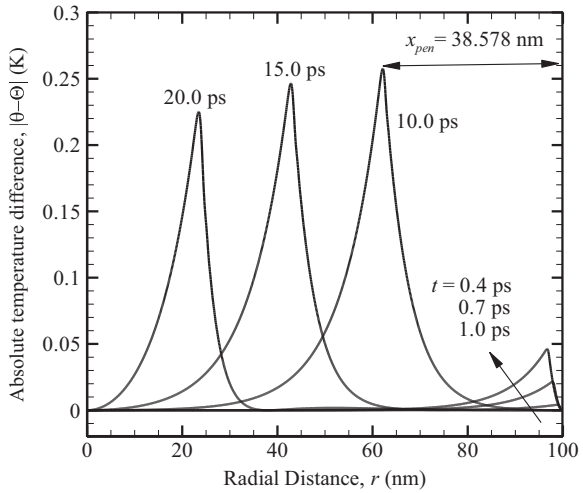

FIG. 10. Absolute difference between equilibrium and nonequilibrium absolute temperature at the interior of 100-nm GNS irradiated with one laser pulse under SPL framework.

For completeness, the absolute difference between nonequilibrium temperature and equilibrium temperature is estimated at various temporal levels, following Eq. (67) and is further depicted in Fig. 10 where the corresponding profile follows the same trend of temperature distribution [see Fig. 7(a)].

On the other hand, a few thermophysical attributes for, e.g., (i) account of no trace(s) of temperature overshooting, (ii) justified direction of heat transfer (from surface towards interior), and (iii) yield of positive definite (equilibrium) entropy production rate at all temporal levels enables the DPL framework to be thermodynamically admissible to the LTE hypothesis. Under short-time picosecond applications, the temperature history retrieved under the DPL framework becomes qualitatively equivalent to "local equilibrium temperature" which finds a suitable macroscopic meaning.

With the consideration and further insertion of an additional phase lag (of temperature gradient, $\tau_T = 90.0$ ps) to the SPL framework, the DPL framework employed for gold appears to be consistent with the LTE hypothesis. But this outcome does not imply the deliberate generalization of the DPL framework to the LTE hypothesis in all situations, since the mathematical nature of the DPL governing energy equation ranges largely between wave to overdiffusion, depending severely on the lag ratio, LR($=\tau_T/2\tau_q$) [25,43]. Hence the LR singly has a profound effect on temperature overshoot and entropy generation characteristics. Keeping thermophysical properties (k,ρ,c) unaltered, with reference to $\tau_q = 8.5$ ps, influence of the LR, varying from 0 (SPL) to 1 (overdiffusion), on temporal temperature rise, heat flux distribution, equilibrium and nonequilibrium entropy production rate, and absolute temperature difference (if any) are investigated. An increase of LR further leads to the following observations: (i) the temperature overshoot is found to be lowered, (ii) the negative entropy production rate (equilibrium), witnessed within the zone of overshoot (surface to x_{pen}), is decayed, (iii) the entropy production rate under the EIT framework is decreased retaining non-negative magnitudes, signifying thermodynamic consistency for all values of LRs, (iv) the absolute numerical difference between equilibrium and nonequilibrium temperature is decreased with maximum magnitude being witnessed for LR = 0 (SPL), and last (v) the sharp wave fronts (discontinuities) observed under the SPL framework are observed to be smeared (diffused). With the increase of LR from 0.5 onwards, the temperature history is observed to be free from overshooting with non-negative magnitude of entropy production rate (equilibrium) retained. All the results, with reference to $t = 10$ ps, are depicted in Fig. 11.

Based on the magnitudes of τ_T and τ_q adopted, the magnitude of LR was considered to be 5.29 (overdiffusion) for the GNS under consideration. Therefore, the results were found to be admissible to the LTE hypothesis under the CIT framework, whereas the DPL framework with smaller LR might not extend the same thermodynamic characteristics.

D. Irradiation with multiple series of pulses and pulse train

We have further extended the applications of reported numerical methods to obtain temporal temperature rise and heat flux distribution of three different cases of laser irradiation: (i) series of two laser pulses, (ii) series of three laser pulses, and (iii) laser pulse train. The corresponding temporal intensity distribution is presented in Eqs. (9) and (10) and is further depicted in Figs. 2(b)–2(d) respectively. Results obtained from all the numerical schemes (see Fig. 12) match extremely well with each other for all situations where no overshooting of temperature is witnessed within the interior of the GNS. Physically it signifies that the surface of the GNS shows maximum temperature rise and heat is observed to transfer from surface to interior, yielding nonpositive magnitudes of (equilibrium) entropy production rate for all spatiotemporal domains. On account of more numbers of intensity peaks (local maxima of intensity) and larger temporal spread of intensity distribution, the maximum temperature rise of the GNS surface and the corresponding peaking time is observed to be enhanced for irradiation with multiple series of pulse and pulse train.

Because of the presence of a maximum number of intensity peaks, possessing a magnitude ($1.037\, I_{\max}$) higher compared to other sources, the maximum temperature at the surface is observed to be largest for irradiation of a GNS with a series of three laser pulses. Similarly, the maximum peaking time is witnessed during irradiation of a GNS with a laser pulse train, on account of the maximum separation of two peaks of pulses ($4t_p$) leads to a maximum spread of temporal intensity distribution ($8t_p$). The maximum temperature rise and the corresponding peaking time predicted by all the numerical schemes for all laser irradiation sources are presented in Table III.

E. Effect of change of laser fluence and radius of GNS on thermal lagging

Previous laser-heating experiments [2–7,42,43] reveal that for small time (picoseconds) transients, the change of reflectivity and electron temperature of the surface was observed to vary linearly with the change of laser fluence during ultrafast transient heating of gold film. Following this nature, it was concluded that having being normalized by their corresponding maximum magnitudes, both electron temperature and

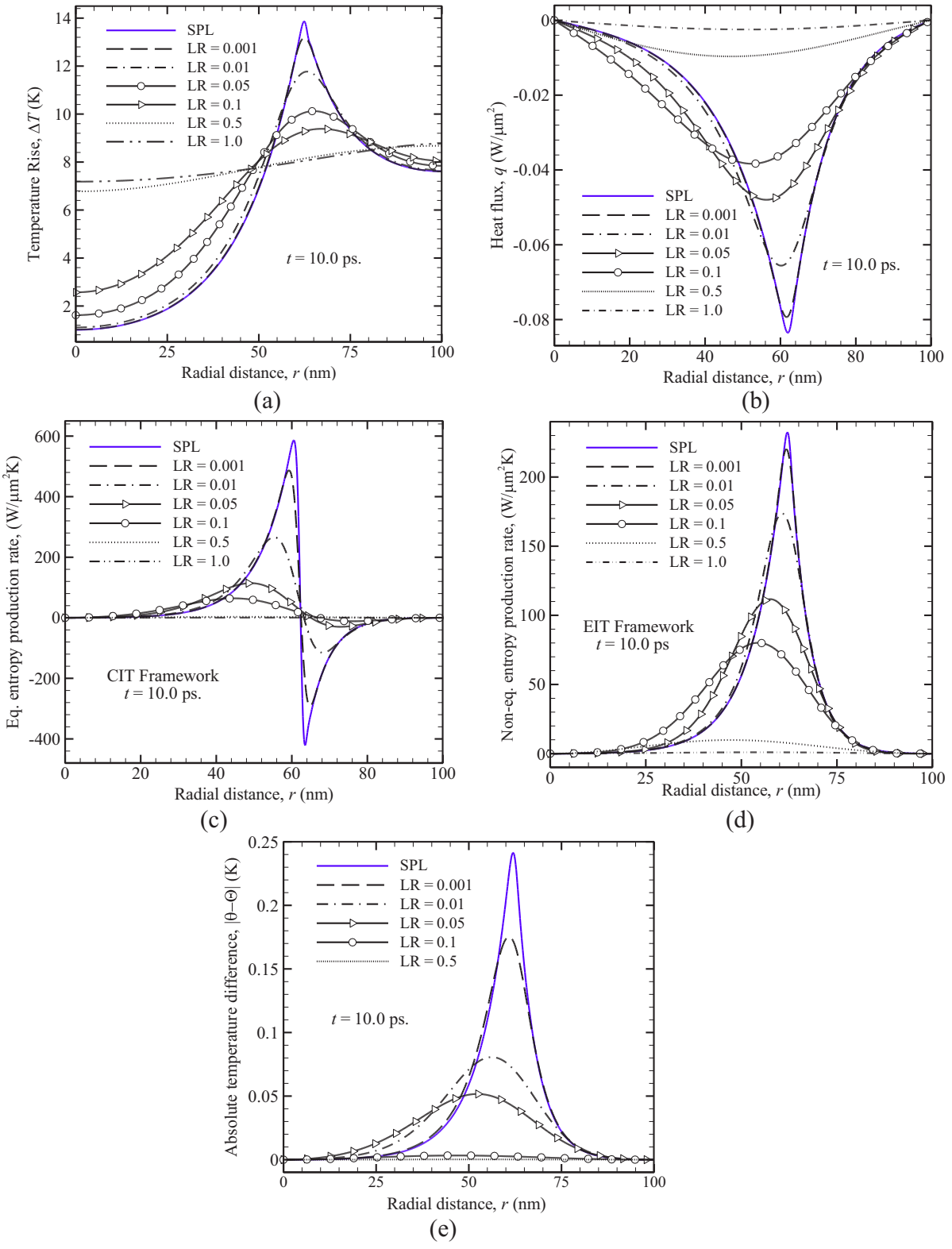

FIG. 11. Effect of lag ratio on (a) temperature rise, (b) heat flux, (c) equilibrium, and (d) non equilibrium entropy production rate, (e) absolute equilibrium and non equilibrium temperature difference.

reflectivity change at the surface retain the same magnitude during picoseconds transients. Inspired by this outcome, we have examined the nature of temperature rise retrieved from the DPL framework with a change of laser fluence ($0-40\,\mathrm{J/m^2}$), at various locations (from surface to center) of a GNS irradiated by all four laser-irradiation sources in Fig. 13. The time of observation was selected to be the respective peaking time of laser irradiation source(s).

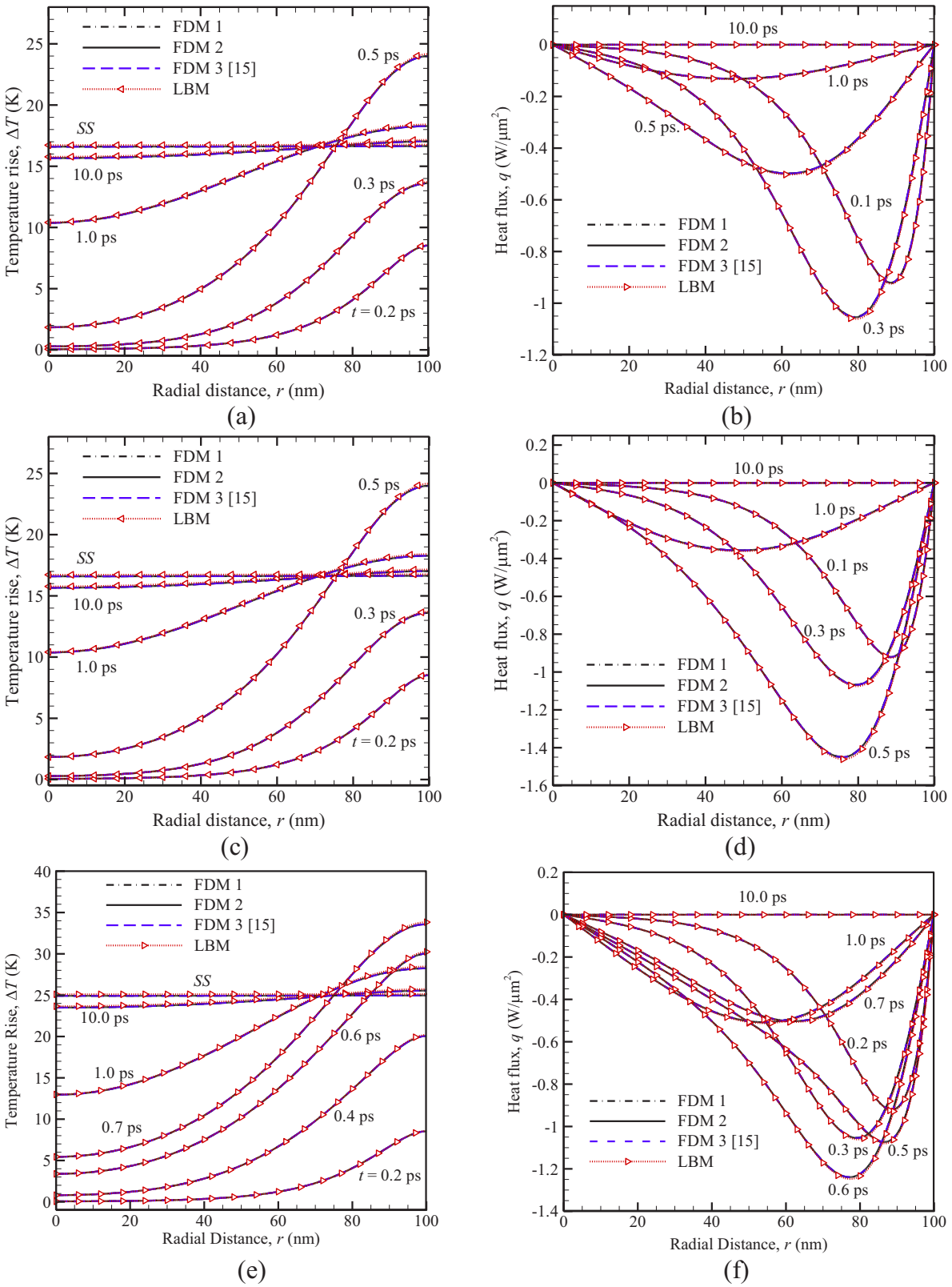

FIG. 12. Temporal temperature rise and heat flux distribution of a 100-nm GNS irradiated with series of (a),(b) two, (c),(d) three, and (e),(f) pulse train under DPL framework respectively by all the numerical schemes.

It is observed that the temperature rise at various location(s) of a GNS varies linearly with change of laser fluence. Therefore, similar to the electron temperature of two step models, the temperature change retrieved by the DPL framework can be quantitatively related to the change of reflectivity change of a GNS during small time response,

TABLE III. Prediction of maximum temperature (ΔT_{max}) and the corresponding peaking time (t_{max}) at the surface of (a) 50-nm, (b) 100-nm, (c) 150-nm, (d) 200-nm GNS irradiated with one laser pulse, series of two pulses, series of three pulses, and pulse train under DPL framework by all the numerical schemes.

One pulse																
Radius:	$L = 50$ nm				$L = 100$ nm				$L = 150$ nm				$L = 200$ nm			
Schemes:	LBM	FDM 1	FDM 2	FDM 3 [15]	LBM	FDM 1	FDM 2	FDM 3 [15]	LBM	FDM 1	FDM 2	FDM 3 [15]	LBM	FDM 1	FDM 2	FDM 3 [15]
ΔT_{max}(K)	14.814	14.805	14.809	14.809	13.957	13.896	13.900	13.900	13.693	13.689	13.693	13.693	13.558	13.559	13.556	13.567
t_{max}(ps)	0.280	0.280	0.280	0.280	0.270	0.270	0.270	0.270	0.270	0.270	0.270	0.270	0.270	0.265	0.270	0.270
Series of two pulses																
ΔT_{max}(K)	27.958	27.953	27.956	27.956	24.748	24.745	24.749	24.749	23.979	23.972	23.978	23.978	23.601	23.597	23.595	23.604
t_{max}(ps)	0.475	0.475	0.475	0.475	0.465	0.465	0.465	0.465	0.460	0.460	0.460	0.460	0.460	0.460	0.460	0.460
Series of three pulses																
ΔT_{max}(K)	40.898	40.883	40.885	40.885	34.594	34.583	34.599	34.589	32.913	32.905	32.911	32.913	32.133	32.131	32.123	32.140
t_{max}(ps)	0.675	0.675	0.675	0.675	0.665	0.665	0.665	0.665	0.660	0.660	0.660	0.660	0.660	0.660	0.660	0.660
Pulse train																
ΔT_{max}(K)	13.558	13.559	13.556	13.567	23.711	23.848	23.688	23.688	22.597	22.588	22.595	22.595	22.156	22.159	22.152	22.152
t_{max}(ps)	0.270	0.265	0.270	0.270	0.670	0.670	0.670	0.670	0.665	0.665	0.665	0.665	0.665	0.665	0.665	0.665

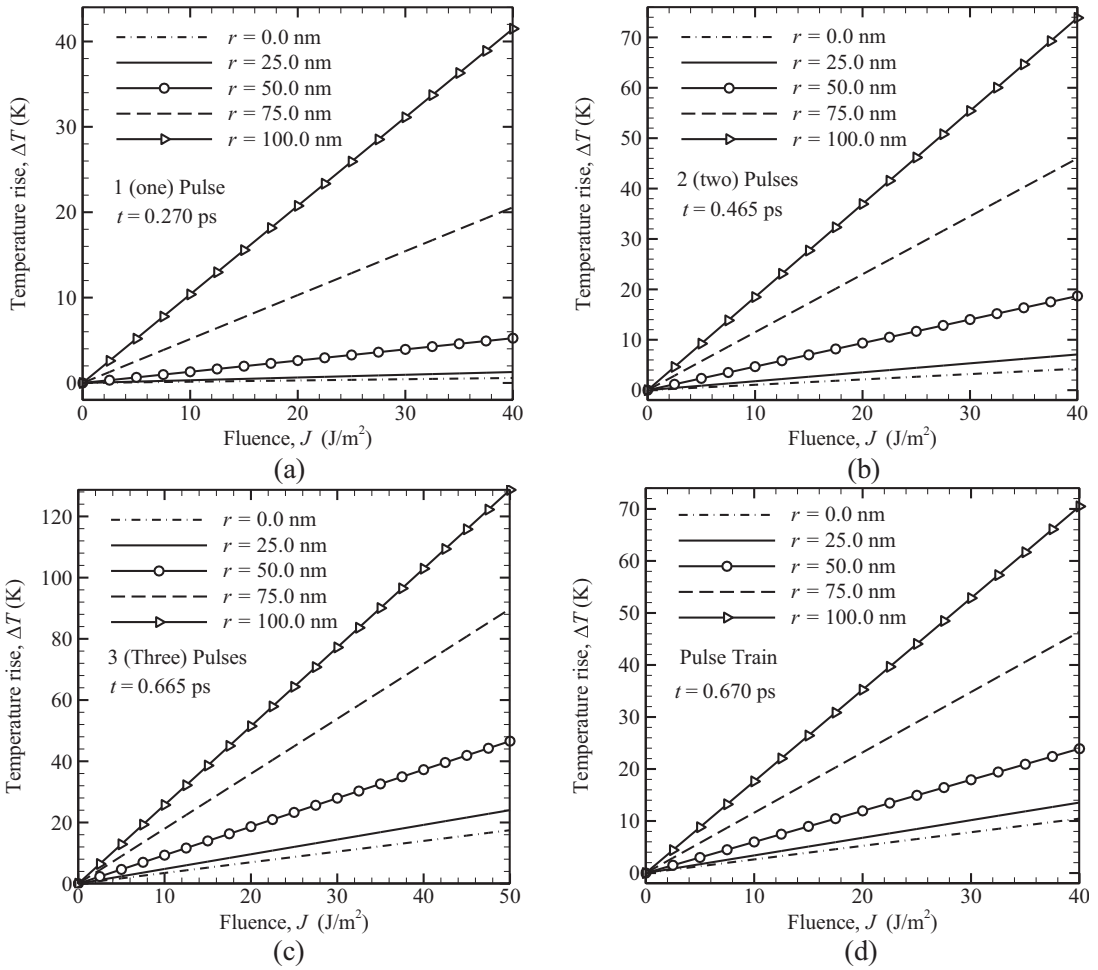

FIG. 13. Temperature rise at various interiors ($\frac{r}{L} = 0.0, 0.25, 0.50, 0.75, 1.0$) of 100-nm GNS vs laser fluence for (a) one, series of (b) two, (c) three laser pulses, and (d) laser pulse train under DPL framework.

$(\Delta T/\Delta T_{\max}) = (\Delta R/\Delta R_{\max})$. Motivated by this observation, a GNS of various radius $L = 50$, 100, 150, and 200 nm are considered and further, transport and lagging characteristics of thermal energy at various radial locations $(r/L) = 0.0$, 0.25, 0.5, 0.75, and 1.0 are illustrated in terms of normalized temperature change, $(\Delta T/\Delta T_{\max})$. During irradiation with a single laser pulse (Fig. 14), the maximum normalized temperature (reflectivity) change is witnessed on the GNS surface with the presence of a peak (local maxima) at the respective peaking time. Because of transfer of thermal energy from the surface towards the interior, the peak observed at the surface starts getting diffused at the interior locations and the corresponding peaking time shifts further rightwards.

For a GNS of smaller radius, $L = 50$ nm, it is observed that normalized temperature changes at various radial locations are closely packed with each other, signifying a uniform temperature response and marginal change of temperature gradient along the radial direction with a slight shift of peaking time. With the increase of radius, temperature response becomes nonuniform with enhancement of spacing of corresponding normalized temperature profiles, attributed to the higher temperature gradients along the radial direction. However, it can be noted that the normalized temperature profiles at $(r/L) = 0$ and 0.25 are found to be closely packed compared to profiles observed at other radial locations. Since a zero temperature gradient is imposed as a boundary condition at the center and surface of a GNS [Eq. 5(b)] with transportation of thermal energy towards the interior, the temperature gradient increases from the surface towards the interior and further adjusts itself to attain "zero" magnitude at the center. This reveals the observation of a smaller temperature gradient in the neighborhood of the center of the GNS.

The higher temperature gradient witnessed in a GNS of larger radius physically signifies transportation of a larger amount of thermal energy from the surface towards the interior. Therefore, enhancement of the GNS radius leads to the decay of maximum temperature rise at the surface (cf. Table III). This trend of a drop of maximum temperature of the surface with an increase of radius is also retained for irradiation of the GNS with other source terms. The temperature peak observed at the GNS surface was observed to spread more towards the interior with a shift of peaking time towards the right with the increase of radius. However, the peaking time at the surface $(r = L)$ is observed to remain almost invariant with a change of radius of the GNS (i.e., for a 50–200-nm GNS). This observation indicates that the peaking time of surface is uninfluenced by the increase of the radius of the GNS (cf. Table III), albeit the interior peaking time is influenced effectively because of

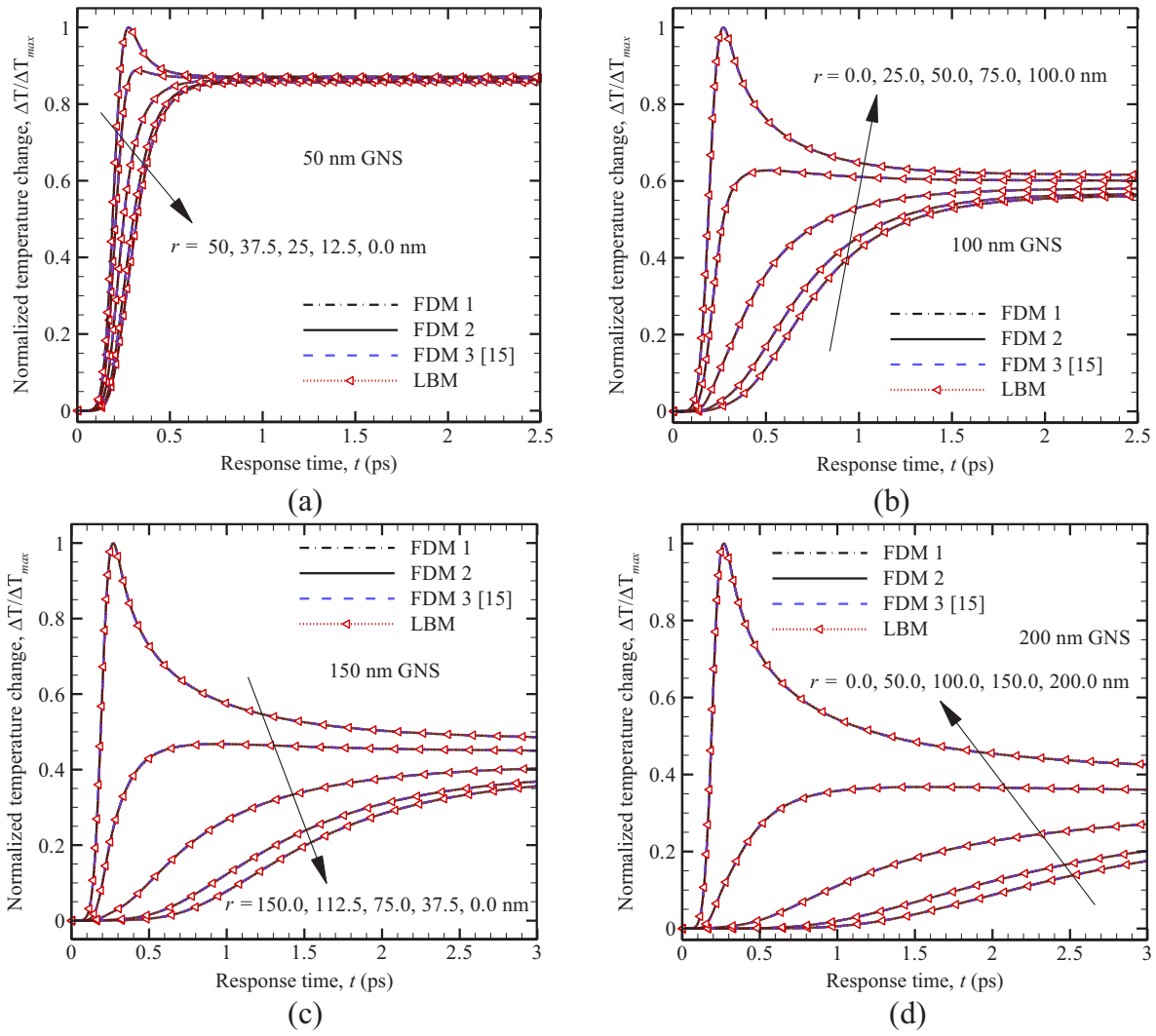

FIG. 14. Normalized temperature change at various interiors ($\frac{r}{L} = 0.0, 0.25, 0.50, 0.75, 1.0$) of (a) 50-nm, (b) 100-nm, (c) 150-nm, (d) 200-nm GNS irradiated with one laser pulse.

appreciable thermal lagging (relaxation and thermalization). Further investigations with a series of two pulses, depicted in Fig. 15, reveals the presence of two peaks on the normalized temperature change profile, at the surface of the GNS.

This observation is an outcome of the temporal intensity distribution [Fig. 2(b)] where, after attaining the first peak (local maxima) (1.018 $I_{\max}$) at $t = 2t_p$, the magnitude of intensity decreases, attends a local minima (0.736 $I_{\max}$) at $t = 3t_p$, and finally increases subsequently to attend the second peak (local maxima) (1.018 $I_{\max}$) at $t = 4t_p$. Similarly, irradiation with the series of three pulses [Fig. 2(c)] results in the presence of three peaks on the normalized temperature change profile, at the GNS surface (cf. Fig. 16).

For both cases (Figs. 15 and 16), on account of the transfer of thermal energy towards the interior, the intermediate peak(s) get(s) diffused completely when reaching the center. In addition to a nonuniform temperature profile, a GNS of larger radius exhibits a significant smearing of the intermediate peak(s). The last irradiation source, i.e., the laser pulse train [Fig. 2(d)] is characterized by two aspects: (i) a maximum intermediate drop of intensity ($I_{\max}$ to zero) at $t = 4t_p$ following the presence of the first peak, and (ii) a maximum temporal distance between subsequent peaks ($4t_p$). This triggers the spread of the intermediate peak on the normalized temperature change at the surface of the GNS. Therefore, compared to irradiation with previous sources, the dominant presence of the intermediated peak is observed at the surface (cf. Fig. 17).

However, with the rise of the radius of the GNS, temperature peaks are observed to diffuse and $L = 200$ nm shows a negligible presence of intermediate peak at the interior locations [Fig. 17(d)]. These results highlight the appreciable presence of thermal lagging (with more transportation and penetration of thermal energy), when the radius of the GNS is enhanced. However, closer viewing of the temperature response reveals that the continuous increase of the GNS radius does not necessarily enhance thermal lagging equally at the same rate for all cases. For, e.g., with reference to surface temperature response between $L = 50$ nm and 100 nm, temperature response between $L = 150$ nm and 200 nm is observed to be closely packed for all laser-irradiation cases.

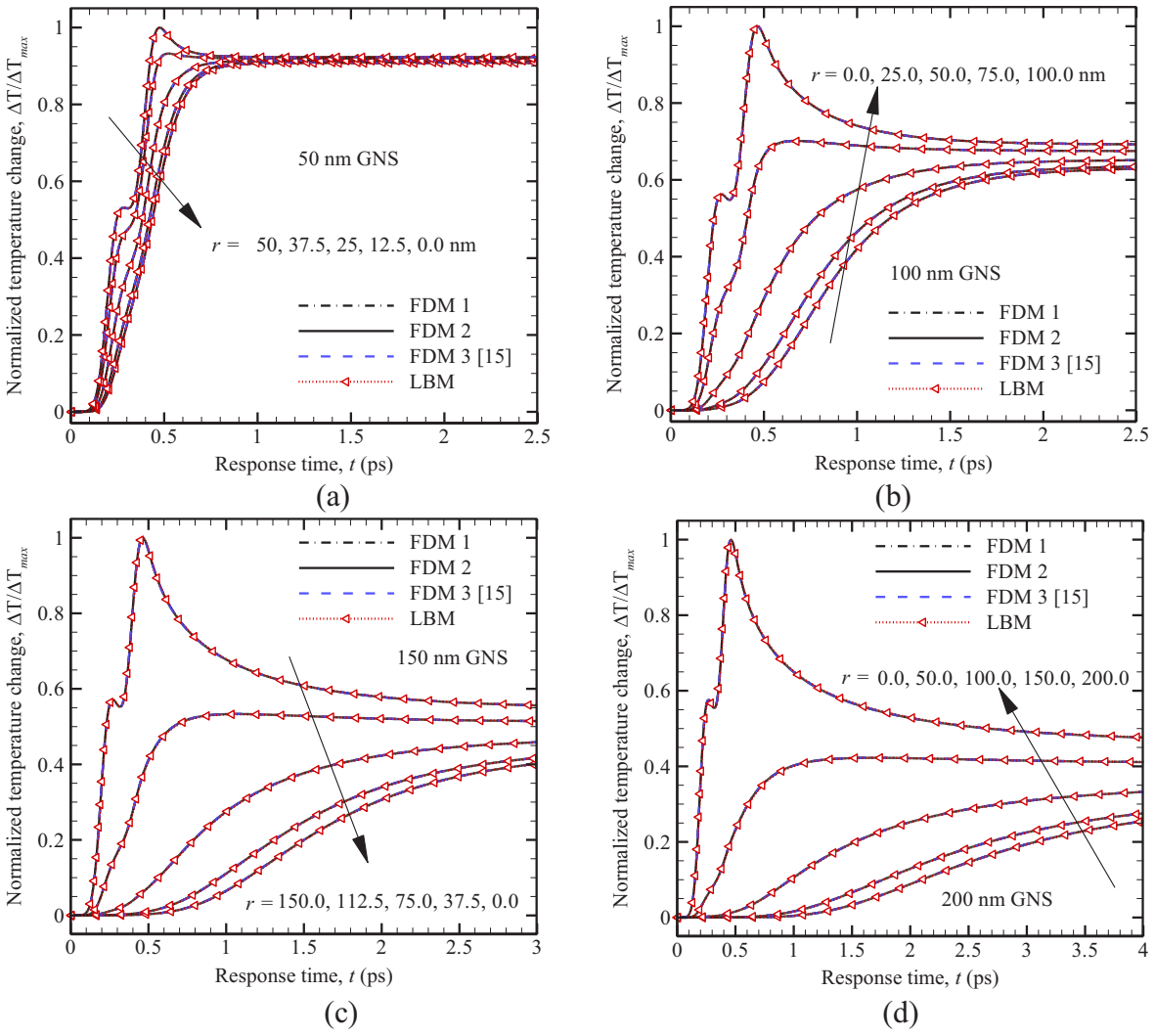

FIG. 15. Normalized temperature change at various interiors ($\frac{r}{L} = 0.0, 0.25, 0.50, 0.75, 1.0$) of (a) 50-nm, (b) 100-nm, (c) 150-nm, (d) 200-nm GNS irradiated with series of two laser pulses.

F. Role of effective thermal conductivity (temperature dependence and size effect)

It is crucial to address that the analysis of microscale heat transfer by macroscopic non-Fourier frameworks does not explicitly take any spatiomicroscopic effects (for, e.g., the inclusion of mean free path or Knudsen number in mathematical formulation) into account. With the shortening of length scale (reduced to the order of mean effective path), the number of molecular collisions (between energy carriers) gets successively reduced and the ballistic behavior in heat transfer becomes pronounced. Although this highly nonlocal phenomenon observed in a GNS is qualitatively addressed by the DPL framework with a macroscopic temperature [satisfying the CIT framework with yield of non-negative (equilibrium) entropy production rate], the definition of thermal conductivity was hardly revised to be an "effective" one. Thermal conductivity taken into the majority of studies [15,17,28,43] involving non-Fourier two-step or SPL or DPL frameworks is actually the electron thermal conductivity (k_e) whereas the conductivity of metallic lattice was largely neglected. Later, single or bulk thermal conductivity (k), employed by Qiu and Tien [7], was related to electron thermal conductivity (k_e) as a function of temperature as follows:

$$k_e \equiv k\left(\frac{T_e}{T_l}\right). \tag{65}$$

In Eq. (65), T_e and T_L are the electron temperature and lattice temperature respectively and the relation becomes valid when the electron temperature is considered much lower than the Fermi temperature [7]. With the accomplishment of thermal equilibrium (i.e., thermalization between electron temperature and lattice temperature, $T_e \approx T_l$), the bulk thermal conductivity eventually becomes equal to the electron thermal conductivity. However, under short-pulse heating, for small time (picoseconds) transients, the majority of the penetrated thermal energy is transferred to the interior via free electrons leading to larger electron temperature; $T_e \gg T_l$. Therefore, following the correlation presented in Eq. (65), thermal conductivity (k) under picosecond transient should become less than the conventional single or bulk thermal conductivity. Further, with the significant enhancement (or reduction) of spatial dimension(s) of physical domain, a larger (or smaller)

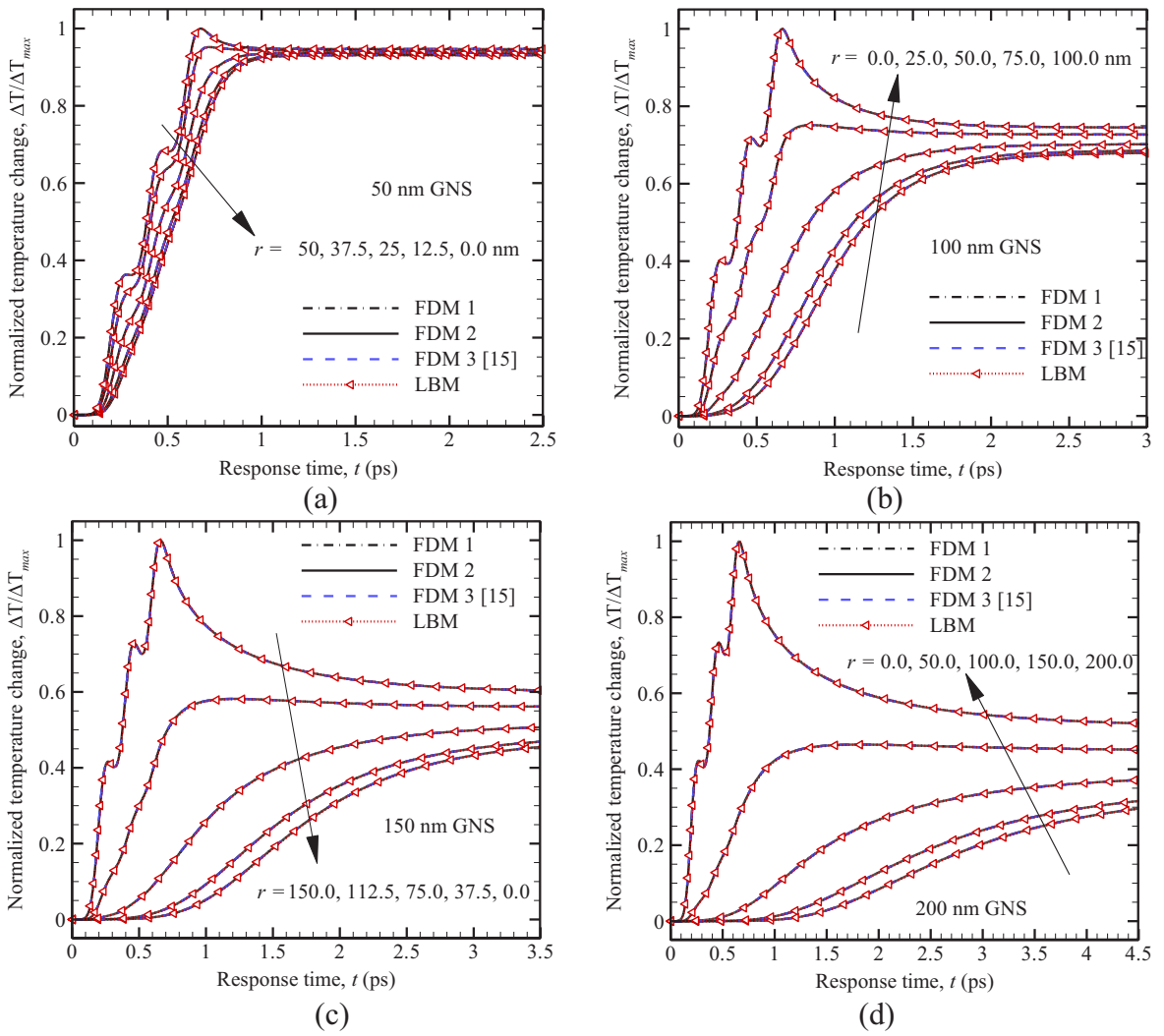

FIG. 16. Normalized temperature change at various interiors ($\frac{r}{L} = 0.0, 0.25, 0.50, 0.75, 1.0$) of (a) 50-nm, (b) 100-nm, (c) 150-nm, (d) 200-nm GNS irradiated with series of three laser pulses.

number of interactions of energy carriers (viz. phonon and free electron) commence at a given instant of time. Under these circumstances, the number of collisions experienced by the energy carrier(s) must influence the thermal conductivity which eventually ceases to remain a sole function of electron thermal conductivity alone.

Considering these circumstances and the following previous lead efforts [38,39,42,51], we are formulating an expression of effective thermal conductivity (k_{eff}) as functions of (i) bulk thermal conductivity (temporal temperature dependence form) [42] and (ii) the Knudsen number Kn, based on the radius of a GNS (defined to be the ratio of mean free path of collision and length scale) as follows [38]:

$$k_{\text{eff}}(\Lambda_1, \Lambda_2) = \Lambda_1[k(T(r,t))] \cdot \Lambda_2(\text{Kn}). \tag{66}$$

In Eq. (66), Λ_1 and Λ_2 are respective functions of temperature dependent (bulk) thermal conductivity and Knudsen number and further are formulated mathematically as follows:

$$\Lambda_1[k(T(r,t))] = k_b\left(\frac{T(r,t)}{T_o}\right)^{0.6}, \tag{67a}$$

$$\Lambda_2(\text{Kn}) = \left(\frac{\sqrt{1+4\pi^2\text{Kn}^2}-1}{2\pi^2\text{Kn}^2}\right); \quad \text{Kn} = \left(\frac{\lambda_m}{L}\right). \tag{67b}$$

In Eq. (67a), k_b is the bulk thermal conductivity at initial (room) temperature T_0(=300 K). Since at picosecond transient the problem is thermophysically unsteady, Λ_1 in Eq. (67a) encompasses the unsteady effect(s). However, Λ_2 in Eq. (67b) does not inherit any unsteady feature(s) [38] and solely remains dependent on the size (radius) of the physical domain, emulated by Kn. In this case, for a GNS of given radius, Kn is conceived to be a constant (although for high temperature applications, it can strongly depend on a change of temperature). With the enlargement of physical length scale of the problem, i.e., a very low Knudsen number; $\text{Kn} \ll 1$, we observe $\Lambda_2 \to 1$. This signifies that the independence of effective thermal conductivity from the size (radius) of the GNS and heat

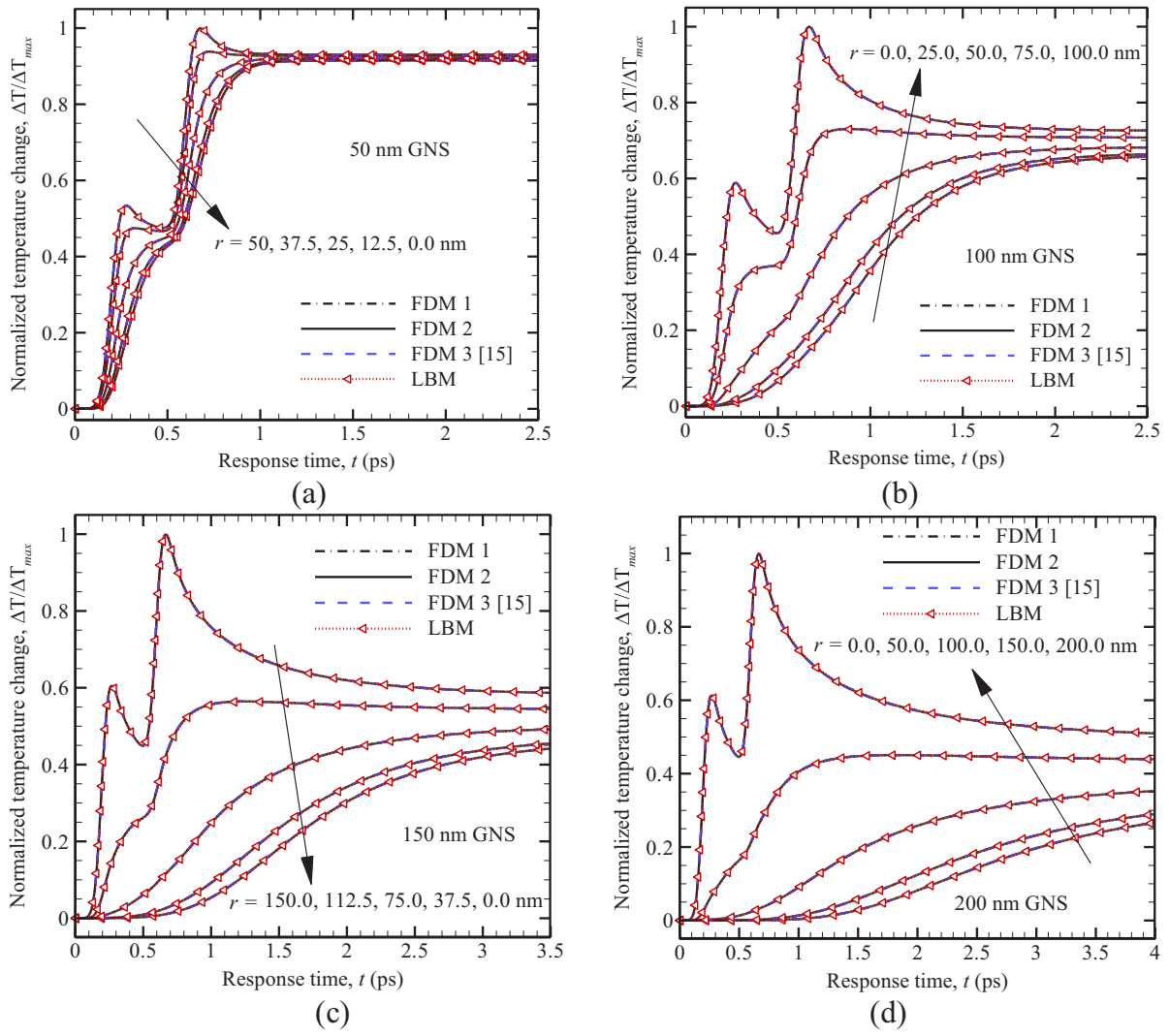

FIG. 17. Normalized temperature change at various interiors ($\frac{r}{L} = 0.0, 0.25, 0.50, 0.75, 1.0$) of (a) 50-nm, (b) 100-nm, (c) 150-nm, (d) 200-nm GNS irradiated with laser pulse train.

transfer characteristics eventually turns to be thermophysically diffusive, rather than ballistic. Since, in the current situation, the radius of the GNS is varied from 50 to 200 nm and the mean effective path λ_m is considered to be 25 nm [52], the magnitude of Kn varies from 0.125 to 0.5 with Λ_2 varying from 0.465 to 0.880. Therefore, k_{eff} becomes clearly less as compared to the corresponding magnitude of k_b. It is worth discussing that in situations where Kn appears to be greater than 1, the source term on account of laser-material interaction has to be modeled by appropriate frameworks (e.g., the phonon-radiative transfer equation) rather than implementing Beer's law [as considered here in Eq. (6)].

In order to understand (i) the characteristics of temperature response while adopting effective thermal conductivity (instead of bulk thermal conductivity) and (2) temporal distribution of effective thermal conductivity at picosecond transient, computation(s) are performed for a GNS of radius $L = 50$, 100, 150, and 200 nm, irradiated with a short-pulse laser. However, inclusion of temperature dependence in Eq. (66) turned the governing algebraic equation(s) (derived from various schemes in Sec. II) highly nonlinear. Therefore, effective thermal conductivity needs to be further linearized as follows [42]:

$$[k_{\text{eff}}(\Lambda_1,\Lambda_2)]_i^{m+1} = \{\Lambda_1[k(T(r,t))]\}_i^{m+1} \cdot [\Lambda_2(\text{Kn})]_i^{m+1}$$
$$= k_b\left(\frac{T_i^m}{T_o}\right)^{0.6} \cdot \Lambda_2(\text{Kn})$$
$$\left[\because [\Lambda_2(\text{Kn})]_i^{m+1} = \Lambda_2(\text{Kn})\right]. \quad (68)$$

In Eq. (68), for a GNS of given radius Λ_2 remains a constant (i.e., independent of physical and temporal index i and m respectively). In this entire study, we further assume that (i) other than k, remaining intrinsic thermophysical properties (τ_q, τ_T, ρc) are temperature averaged (as depicted in Sec. III A) and (ii) effective thermal conductivity is independent of the imposed frequency of short-pulse laser. All the results obtained for a GNS of various radii are subsequently depicted in Fig. 18.

For all the cases, the peaking time of the surface of the GNS is observed to remain invariant to the inclusion of effective thermal conductivity. However, the surface temperature response past the local maxima is found to retain a lower magnitude compared to the temperature response witnessed

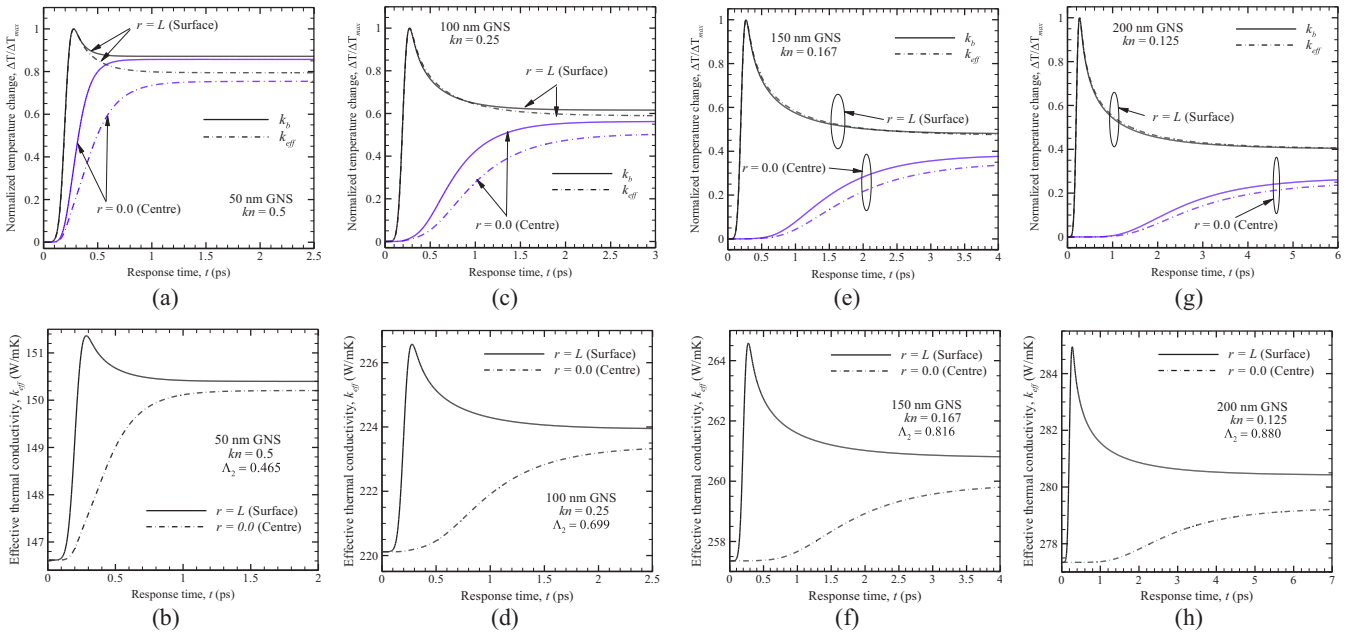

FIG. 18. Normalized temperature change and temporal variation of effective thermal conductivity at surface and center of (a),(b) 50-nm, (c),(d) 100-nm, (e),(f) 150 nm, and (g),(h) 200-nm GNS respectively: the role of effective thermal conductivity.

considering bulk thermal conductivity. This is because for $0.125 \leqslant \mathrm{Kn} \leqslant 0.5$, effective thermal conductivity is always lower than the bulk thermal conductivity. Since volumetric effects are more pronounced on the interior ($r = 0.0$) of a GNS (Sec. III E), the thermophysical response at the center is observed to deviate (lower) significantly with respect to the conventional situation where bulk thermal conductivity was considered.

With reference to Fig. 18 and observations noted while investigating thermal lagging in Sec. III E, we first summarize the benchmark thermophysical aspect(s) when the radius of a GNS is enlarged. With the rise of the radius of GNS, (i) the corresponding Knudsen number decreases, (ii) the magnitude of the effective thermal conductivity simultaneously increases [cf. Figs. 18(b), 18(d), 18(f), and 18(h)] (though in the present case, it still remains much less than the bulk thermal conductivity), and, last but not least, (iii) the volumetric lagging phenomenon becomes appreciable with the presence of larger phonon-electron interaction(s). Therefore, the temporal temperature response witnessed for both cases (effective and bulk thermal conductivity) is found to remain closed with the rise of the GNS radius (e.g., the temperature response at the surface with effective thermal conductivity is almost superimposed with the temperature response at the surface considering bulk thermal conductivity). Interestingly, it is noted that the temporal variation of the effective thermal conductivity profile follows almost the same trend of temporal normalized temperature change profile (with effective thermal conductivity).

For a GNS of a given radius, the peaking time of effective thermal conductivity also remains identical to the respective peaking time of temperature response at the surface and center. Progressive relaxation and thermalization result in the enlargement of spacing between the corresponding effective thermal conductivity profiles at the surface and center (similar to temperature profiles) for a GNS of higher radius (lower Knudsen number). Since pronounced thermal lagging facilitates a larger temperature gradient with higher transportation of thermal energy towards the interior (cf. Sec. III E), the k_{eff} distribution at the surface varies (decays past the local maxima) significantly when the radius of GNS is enlarged. On the other hand, a lower (rate of) temperature rise at the interior eventually results in a timidly varying k_{eff} with a further shift of peaking time towards the right (the center of a GNS).

G. Convergence characteristics and CPU time

With the background of accuracy reported in Sec. III A, efficiency of the schemes to solve the DPL governing energy equation with the laser irradiation source term is assessed by studying the convergence characteristics as well as the corresponding CPU time per unit step. For irradiation of a GNS with single laser pulse and time step $\Delta t = 0.0001$ ps, the simultaneous decay of error and rise of CPU time are depicted in Figs. 19(a) and 19(b) respectively. From Fig. 19(a), it is observed that the error ξ_2 decays fastest by both LBM and FDM2 schemes up to 3×10^{-9}(650 ps), after which ξ_2 does not change significantly for FDM2. The LBM scheme, however, converges with the same rate and furthermore, a convergence as low as 10^{-12} is obtained. FDM1 shows an excellent rate of convergence (the same as that of FDM2 and LBM) up to 240 ps, beyond which ξ_2 remains almost constant and does not converge beyond 3×10^{-7}(lowest among all the schemes). Convergence of FDM3 [15] is found to remain in between FDM1 and FDM2 in most of the situations.

From Fig. 19(b), it is observed that CPU time increases linearly with physical time (number of iterations) for all schemes, with the lowest slope seen in the LBM scheme. At various levels of convergence, the CPU time of LBM is found to be 5–12 times faster than in other FDM schemes, signifying a

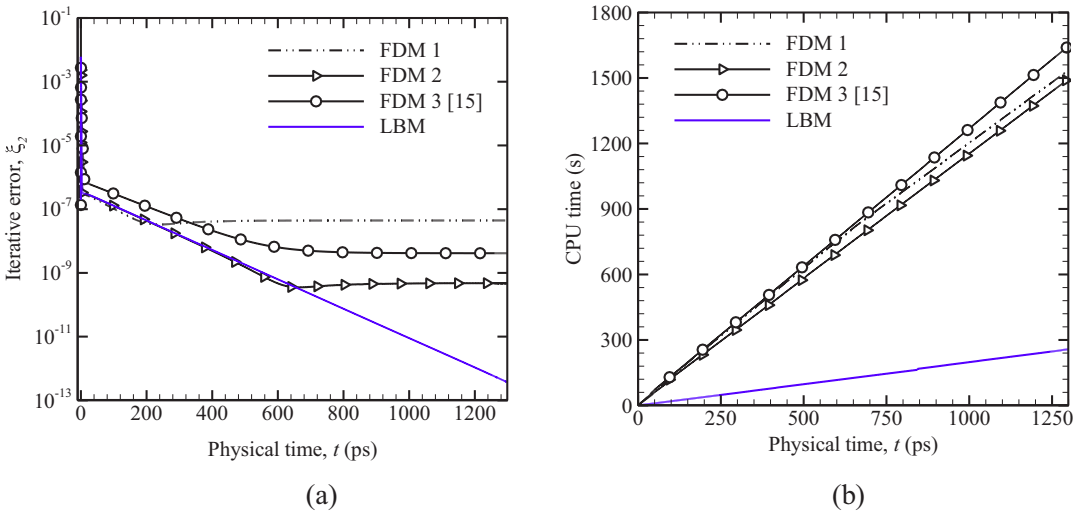

FIG. 19. (a) Convergence history with physical time, (b) CPU time vs physical time under DPL framework for all the numerical schemes.

lower computational cost per iteration (time step). Since all the three level, implicit FDM schemes are solved by the same linear solver (TDMA), CPU time does not vary appreciably. Among the FDM schemes, the maximum computational time and slope is observed by the FDM3 [15] scheme for all situations and the minimum is observed for FDM1. All the computations are performed in a Linux operating system with 20 GB RAM. For a broad scale of iterations performed, results show the computational superiority of the LBM scheme to the remaining FDM schemes, in terms of both aspects of convergence and CPU time.

IV. CONCLUSION

In this article, a brief numerical study is accomplished to illustrate the temperature history and thermal lagging characterization of a gold nanosphere (GNS) irradiated with femtosecond laser pulse(s) by non-Fourier SPL and DPL frameworks such that the problem could be viewed as a delayed response in macroscale. LBM schemes and FDM schemes were employed to obtain the correct temperature distribution. In order to understand the qualitative meaning of single-variable temperature defined by these frameworks and their qualitative thermodynamic interpretation in the context of thermophysical anomalies like overshooting, entropy generation characteristics by the frameworks of classical and irreversible thermodynamics are presented. Useful observations, conclusions, and future work from the numerical study are presented briefly as follows:

(i) At the subpicosecond temporal domain, effective penetration of thermal energy within the interior of a GNS is observed under the DPL framework, whereas under the SPL framework, thermal energy is contained within the neighborhood of the GNS surface resulting in a higher temperature rise and a larger peaking time of the GNS surface. The ineffective transportation of thermal energy observed under the SPL framework was further justified by the calculation of the penetration depth of a thermal wave. With the increase of time, the temperature discontinuity propagates inwards and overshooting within the GNS, characterized by adverse temperature gradient, was noticed.

(ii) Instead of the presence of an adverse temperature gradient, heat was observed to transfer from the surface towards the interior (unlike with Fourier's law where a sense of heat-flux and temperature gradient were mutually exclusive). Thermodynamic analysis further reveals that the zone of temperature overshoot is characterized by a negative (equilibrium) entropy production rate (under the CIT framework) violating LTE, whereas, under the EIT framework, a nonzero entropy production rate is observed at all temporal levels. It can be concluded that temperature obtained under the SPL framework is qualitatively equivalent to a nonlocal thermal wave (with no appreciable equilibrium interpretation).

(iii) The DPL framework, free from temperature overshooting, satisfies the LTE hypothesis by yielding a positive definite (equilibrium) entropy production rate. The temperature history retrieved in the paradigm of DPL qualitatively becomes equivalent to (local) equilibrium temperature. Results at all temporal levels under the DPL framework show the GNS surface to attain the highest temperature.

(iv) It is important to infer that the DPL framework for all magnitudes of LR is not globally admissible to the LTE framework. For LR < 0.5, temperature overshooting is observed yielding a negative equilibrium entropy production rate. Since for gold, LR(=5.29) is considered to be greater than 0.5, consistency with the LTE framework is observed. However, this observation is limited to fixed thermal diffusivity α and heat capacity ρc.

(v) Studying the linear rise of temperature with laser fluence under the DPL framework, under spherical coordinate geometry, it was concluded that the normalized temperature change is equal to the normalized reflectivity change. The effect of the change of radius of the GNS on thermal lagging and irradiation with various laser sources was further assessed. It was concluded that with the enhancement of radius, penetration and lagging of thermal energy is more pronounced on account of phonon-electron interaction in space resulting in a nonuniform temperature response. However, thermal lagging is not enhanced appreciably at the same rate for all situations.

(vi) An expression of effective thermal conductivity is formulated considering unsteady (temperature) effect and size (Knudsen number) dependence. The quantitative difference between thermophysical response obtained from situations involving bulk and effective thermal conductivity is illustrated in detail with the change of radius of a GNS. It was concluded that the thermal response(s) obtained considering bulk and effective thermal conductivity vary significantly for a GNS of lower radius (i.e., a higher Kn and a lower k_{eff}). The temporal effective thermal conductivity profile is observed to follow the same trend of temporal normalized temperature response. With the increase of a GNS radius (i.e., lower kn and higher k_{eff}), spacing between the k_{eff} profile at the surface and center enhances progressively on account of pronounced phonon-electron interaction (thermal lagging). We feel that more experimental studies are warranted to judge the rightness of the effective thermal conductivity formulated above and left further, as an open debate.

(vii) Results obtained from four numerical schemes match each other exceedingly well, for all cases. Comparing with an analytical solution, the LBM scheme was observed to yield maximum accuracy for all situations. The LBM scheme was also observed to converge as low as 10^{-12} with minimum CPU time required per time step. The reported FDM scheme (FDM3) appears to be an effective scheme with reasonable accuracy, convergence, and CPU time (superior to the FDM scheme of Dai *et al.* [15], in most of the situations). Maximum temperature rise at the surface and the corresponding peaking time are computed by all the numerical schemes. We feel the temperature history of the GNSs depicted in this work as well as the solution tools (to retrieve the former) will be extremely useful to review numerous applications of nanoscale heat transfer, subjected to short-pulse (femtosecond), high-rate heating (micromanufacturing, nanoscience and noninvasive biological applications, etc.). Though high frequency heating is the focus of attention in this study, the thermal response of gold nanoparticles exposed to small frequency heating also fetches paramount interest for medical applications [53]. The applicability of non-Fourier frameworks to this genre of problems remains an open question.

(viii) In this current analysis, we have considered a GNS illuminated to high-rate short-pulse laser heating. We sincerely believe that the current physical modeling will be highly credible for practical situations (e.g., where the GNS is surrounded by other entities, say, biological tissues or other nanoparticles) where, on account of the presence of the surrounding medium, a laser pulse is irradiated uniformly over the GNS surface with normal incidence. Therefore, the solution tools depicted will be useful to provide a first-hand approximation of temperature rise of a GNS at picosecond transient. However, for more accurate analysis of this genre of problems where a GNS is coupled with entities of different thermophysical attributes, the effect of interfacial condition(s) on thermal energy transport needs to be thoroughly analyzed both quantitatively as well as qualitatively. We are currently investigating the scope of implementing the above reported numerical schemes to efficiently elucidate the role of the interfacial phenomenon on temperature response and thermodynamic characteristics.

ACKNOWLEDGMENTS

The authors would like to express their sincere acknowledgment to the late Professor S. C. Mishra and the referees for extending innumerable suggestions, which eventually helped us to thoroughly improve the quality of the manuscript.

APPENDIX: DETAILED FORMULATIONS OF FINITE DIFFERENCE SCHEMES (FDM1 AND FDM2)

1. FDM1 scheme

For the solution of the current problem using this scheme involving the volumetric laser irradiation source term, Eq. (5) is first integrated between time levels (m) and $(m+1)$ as follows:

$$\int_{(t-\frac{\Delta t}{2})}^{(t+\frac{\Delta t}{2})} \left\{ \frac{\partial}{\partial t}\left[\rho c\left(T + \tau_q \frac{\partial T}{\partial t} \right) - k\tau_T \frac{\partial^2 T}{\partial r^2} - \frac{2k\tau_T}{r}\frac{\partial T}{\partial r} \right] \right\} dt = \int_{(t-\frac{\Delta t}{2})}^{(t+\frac{\Delta t}{2})} \left(k\frac{\partial^2 T}{\partial r^2} + \frac{2k}{r}\frac{\partial T}{\partial r} + G \right) dt. \tag{A1}$$

With m the index for the current time level, the time integration of Eq. (A1) yields,

$$\underbrace{\left[\rho c\left(T + \tau_q \frac{\partial T}{\partial t} \right) - k\tau_T \frac{\partial^2 T}{\partial r^2} - \frac{2k\tau_T}{r}\frac{\partial T}{\partial r} \right]_i^{m+1}}_{\text{I}} - \underbrace{\left[\rho c\left(T + \tau_q \frac{\partial T}{\partial t} \right) - k\tau_T \frac{\partial^2 T}{\partial r^2} - \frac{2k\tau_T}{r}\frac{\partial T}{\partial r} \right]_i^{m}}_{\text{II}}$$
$$= \underbrace{\int_{t=m}^{t=m+1} \left(k\frac{\partial^2 T}{\partial r^2} + \frac{2k}{r}\frac{\partial T}{\partial r} \right)_i dt}_{\text{I}} + \underbrace{\int_{t=m}^{t=m+1} G_i dt}_{\text{II}}. \tag{A2}$$

Time integration performed in Eq. (A2) preserves first order global accuracy in time (left-hand side). Rearranging terms I and II on the left-hand-side, and further evaluating the integration of various terms of the right-hand side by (i) applying a straight line interpolation (trapezoidal integration) between the two consecutive time levels m and $m+1$ of term I (which preserves second

order accuracy in time), and (ii) using the initial value of integrand for the term II, we further obtain

$$\rho c\left[\tau_q\left\{\underbrace{\left(\frac{\partial T}{\partial t}\right)_i^{m+1}}_{\mathrm{I}}-\underbrace{\left(\frac{\partial T}{\partial t}\right)_i^{m}}_{\mathrm{II}}\right\}+\left(T_i^{m+1}-T_i^m\right)\right]-k\tau_T\left\{\left(\frac{\partial^2 T}{\partial r^2}\right)_i^{m+1}-\left(\frac{\partial^2 T}{\partial r^2}\right)_i^{m}\right\}-\frac{2k\tau_T}{r_i}$$
$$\times\left[\left(\frac{\partial T}{\partial r}\right)_i^{m+1}-\left(\frac{\partial T}{\partial r}\right)_i^{m}\right]=\frac{k\Delta t}{2}\left\{\left(\frac{\partial^2 T}{\partial r^2}\right)_i^{m+1}+\left(\frac{\partial^2 T}{\partial r^2}\right)_i^{m}\right\}+\frac{k\Delta t}{r_i}\left\{\left(\frac{\partial T}{\partial r}\right)_i^{m+1}+\left(\frac{\partial T}{\partial r}\right)_i^{m}\right\}+G_i^m\Delta t. \quad \text{(A3)}$$

With the solution space $0\leqslant r\leqslant L$ equally divided into N control volumes, and the FDM nodes placed at the boundaries of the control volumes, the number of grid points considered are $N+1$. Next, in Eq. (A3), for the time derivative terms I and II, a second-order backward difference and a central difference scheme, respectively, is applied. All the spatial derivatives (both first and second order) are discretized using a second order central difference scheme. For all the discretizations performed, second order accuracy in both space and time are preserved. In the discretized forms, these terms are the following:

$$\left(\frac{\partial T}{\partial t}\right)_i^{m+1}=\frac{3T_i^{m+1}-4T_i^m+T_i^{m-1}}{2\Delta t},, \quad \text{(A4)}$$
$$\left(\frac{\partial T}{\partial t}\right)_i^{m}=\frac{T_i^{m+1}-T_i^{m-1}}{2\Delta t}, \quad \text{(A5)}$$
$$\left(\frac{\partial^2 T}{\partial r^2}\right)_i^{m+1}=\left(\frac{T_{i-1}^{m+1}-2T_i^{m+1}+T_{i+1}^{m+1}}{(\Delta r)^2}\right), \quad \text{(A6)}$$
$$\left(\frac{\partial^2 T}{\partial r^2}\right)_i^{m}=\left(\frac{T_{i-1}^{m}-2T_i^{m}+T_{i+1}^{m}}{(\Delta r)^2}\right), \quad \text{(A7)}$$
$$\left(\frac{\partial T}{\partial r}\right)_i^{m+1}=\left(\frac{T_{i+1}^{m+1}-T_{i-1}^{m+1}}{2\Delta r}\right), \quad \text{(A8)}$$
$$\left(\frac{\partial T}{\partial r}\right)_i^{m}=\left(\frac{T_{i+1}^{m}-T_{i-1}^{m}}{2\Delta r}\right). \quad \text{(A9)}$$

Substituting discretization of time and space derivative terms from Eqs. (A4)–(A9) into Eq. (A3), and rearranging the terms, we get the difference equation illustrated in Eq. (37).

2. FDM2 scheme

Instead of integrating between consecutive time levels (m) and $(m+1)$, time integration is simply initiated by integrating Eq. (5) between two intermediate time levels $(m-\frac{1}{2})$ and $(m+\frac{1}{2})$ respectively as follows:

$$\int_{(t-\frac{\Delta t}{2})}^{(t+\frac{\Delta t}{2})}\left\{\frac{\partial}{\partial t}\left[\rho c\left(T+\tau_q\frac{\partial T}{\partial t}\right)-k\tau_T\frac{\partial^2 T}{\partial r^2}-\frac{2k\tau_T}{r}\frac{\partial T}{\partial r}\right]\right\}dt=\int_{(t-\Delta t/2)}^{(t+\Delta t/2)}\left(k\frac{\partial^2 T}{\partial r^2}+\frac{2k}{r}\frac{\partial T}{\partial r}+G\right)dt. \quad \text{(A10)}$$

With m as the index for the current time level, the time integration of Eq. (A10) yields

$$\underbrace{\left[\rho c\left(T+\tau_q\frac{\partial T}{\partial t}\right)-k\tau_T\frac{\partial^2 T}{\partial r^2}-\frac{2k\tau_T}{r}\frac{\partial T}{\partial r}\right]_i^{m+1/2}}_{\mathrm{I}}-\underbrace{\left[\rho c\left(T+\tau_q\frac{\partial T}{\partial t}\right)-k\tau_T\frac{\partial^2 T}{\partial r^2}-\frac{2k\tau_T}{r}\frac{\partial T}{\partial r}\right]_i^{m-1/2}}_{\mathrm{II}}$$
$$=\underbrace{\int_{t=(m-1/2)}^{t=(m+1/2)}\left(k\frac{\partial^2 T}{\partial r^2}+\frac{2k}{r}\frac{\partial T}{\partial r}\right)_i dt}_{\mathrm{I}}+\underbrace{\int_{t=(m-1/2)}^{t=(m+1/2)}G_i dt}_{\mathrm{II}}. \quad \text{(A11)}$$

Terms I and II on the left-hand side in Eq. (A11) are rearranged and similar terms are further grouped together. Integration of terms I and II of the right-hand side are performed by (1) applying a straight line interpolation (trapezoidal integration) between the two consecutive time levels $(m-1/2)$ and $(m+1/2)$ for term I (preserves second order accuracy in time), and (2) using the

initial value of the integrand (at time level m) for the term II, we further obtain

$$\rho c\left[\underbrace{\left(T_i^{m+1/2}-T_i^{m-1/2}\right)}_{\mathrm{I}}+\tau_q\underbrace{\left\{\left(\frac{\partial T}{\partial t}\right)_i^{m+1/2}-\left(\frac{\partial T}{\partial t}\right)_i^{m-1/2}\right\}}_{\mathrm{II}}\right]-k\tau_T\underbrace{\left\{\left(\frac{\partial^2 T}{\partial r^2}\right)_i^{m+1/2}-\left(\frac{\partial^2 T}{\partial r^2}\right)_i^{m-1/2}\right\}}_{\mathrm{II}}-\frac{2k\tau_T}{r_i}$$
$$\times\underbrace{\left\{\left(\frac{\partial T}{\partial r}\right)_i^{m+1/2}-\left(\frac{\partial T}{\partial r}\right)_i^{m-1/2}\right\}}_{\mathrm{IV}}=\frac{k\Delta t}{2}\underbrace{\left\{\left(\frac{\partial^2 T}{\partial r^2}\right)_i^{m+1/2}+\left(\frac{\partial^2 T}{\partial r^2}\right)_i^{m-1/2}\right\}}_{\mathrm{V}}+\frac{k\Delta t}{r_i}\underbrace{\left\{\left(\frac{\partial T}{\partial r}\right)_i^{m+1/2}+\left(\frac{\partial T}{\partial r}\right)_i^{m-1/2}\right\}}_{\mathrm{VI}}$$
$$+G_i^m\Delta t. \tag{A12}$$

In Eq. (A12), term I is interpolated as the average of the preceding and succeeding levels and term II can be further approximated by the central difference scheme. In each of the operations, second order accuracy is preserved,

$$T_i^{m+1/2}-T_i^{m-1/2}=\frac{1}{2}\left(T_i^{m+1}+T_i^m\right)-\frac{1}{2}\left(T_i^m+T_i^{m-1}\right)=\frac{1}{2}\left(T_i^{m+1}-T_i^{m-1}\right) \tag{A13}$$

$$\left(\frac{\partial T}{\partial t}\right)_i^{m+1/2}-\left(\frac{\partial T}{\partial t}\right)_i^{m-1/2}=\frac{T_i^{m+1}-T_i^m}{2\left(\frac{\Delta t}{2}\right)}-\frac{T_i^m-T_i^{m-1}}{2\left(\frac{\Delta t}{2}\right)}=\frac{T_i^{m+1}-2T_i^m+T_i^{m-1}}{\Delta t}. \tag{A14}$$

Similarly, spatial derivatives of temperature at the intermediate levels (terms III–VI) of Eq. (A12) are also interpolated as the average of the preceding and succeeding time levels,

$$\left(\frac{\partial^2 T}{\partial r^2}\right)_i^{m+1/2}=\frac{1}{2}\left[\left(\frac{\partial^2 T}{\partial r^2}\right)_i^{m+1}+\left(\frac{\partial^2 T}{\partial r^2}\right)_i^{m}\right],\quad \left(\frac{\partial^2 T}{\partial r^2}\right)_i^{m-1/2}=\frac{1}{2}\left[\left(\frac{\partial^2 T}{\partial r^2}\right)_i^{m}+\left(\frac{\partial^2 T}{\partial r^2}\right)_i^{m-1}\right], \tag{A15}$$

$$\left(\frac{\partial T}{\partial r}\right)_i^{m+1/2}=\frac{1}{2}\left[\left(\frac{\partial T}{\partial r}\right)_i^{m+1}+\left(\frac{\partial T}{\partial r}\right)_i^{m}\right],\quad \left(\frac{\partial T}{\partial r}\right)_i^{m-1/2}=\frac{1}{2}\left[\left(\frac{\partial T}{\partial r}\right)_i^{m}+\left(\frac{\partial T}{\partial r}\right)_i^{m-1}\right]. \tag{A16}$$

Spatial derivatives in the right-hand side of Eqs. (A15) and (A16) are discretized, as presented in Eqs. (A4)–(A9), and are substituted further into Eq. (A12) to obtain the difference equation illustrated in Eq. (39).

[1] S. I. Anisimov, B. L. Kapeliovich, and T. L. Perel'man, Electron emission from metal surfaces exposed to ultra-short laser pulses, Sov. Phys. JETP **39**(2), 375 (1974).

[2] T. Q. Qiu and C. L. Tien, Short-pulse laser heating of metals, Int. J. Heat Mass Transfer **35**, 719 (1992).

[3] T. Q. Qiu and C. L. Tien, Heat transfer mechanisms during short-pulse laser heating of metals, ASME J. Heat Transfer **115**, 835 (1993).

[4] J. K. Chen, J. E. Beraun, and D. Y. Tzou, A semi classical two-temperature model for ultrasfast laser heating, Int. J. Heat Mass Transfer **49**, 307 (2006).

[5] J. K. Chen and J. E. Beraun, Numerical study of ultrashort laser pulse interactions with metal films, Numer. Heat Transfer, Part A **40**, 1 (2001).

[6] S. D. Brorson, J. G. Fujimoto, and E. P. Ippen, Femtosecond Electron Heat-Transport Dynamics in Thin Gold Film, Phys. Rev. Lett. **59**, 1962 (1987).

[7] T. Q. Qiu, T. Juhasz, C. Suarez, W. E. Bron, and C. L. Tien, Femtosecond laser heating of multi-layer metals–II. Experiments, Int. J. Heat Mass Transfer **37**, 2799 (1994).

[8] C. Cattaneo, A form of heat conduction equation which eliminates the paradox of instantaneous propagation, Comptes Rendus **247**, 431 (1958).

[9] P. Vernotte, Les paradoxes de la theorie continue de l equationdel la Chaleur, Compte Rendus **246**, 3154 (1958).

[10] Z. M. Zhang, T. J. Bright, and G. P. Peterson, Reexamination of the statistical derivations of Fourier's law and Cattaneo's equation, Nanoscale Microscale Thermophys. Eng. **15**, 220 (2011).

[11] A. Agarwal, Higher-order continuum based heat conduction law, INAE Lett. **1**, 35 (2016).

[12] D. Y. Tzou, A unified field approach for heat conduction from macro-to micro-scales, J. Heat Transfer **117**, 8 (1995).

[13] V. I. Zakomirnyi, I. L. Rasskazov, S. V. Karpov, and S. P. Polyutov, New ideally absorbing Au plasmonic nanostructures for biological applications, J. Quantum Spectrosc. Radiat. Transfer **187**, 54 (2017).

[14] I. H. El-Sayed, X. Huang, and M. A. El-Sayed, Selective laser photo-thermal therapy of epithelial carcinoma using anti-EGFR antibody conjugated gold nanoparticles, Cancer Lett. **239**, 129 (2006).

[15] W. Dai, L. Shen, R. Nassar, and T. Zhu, A stable and convergent three-level finite difference scheme for solving a dual-phase-lagging heat transport equation in spherical coordinates, Int. J. Heat Mass Transfer **47**, 1817 (2004).

[16] P. Fischer, N. Karapatis, V. Romano, and H. P. Weber, A model for interaction of near-infrared laser pulse with metal powders in selective laser sintering, Appl. Phys. A **74**, 467 (2002).
[17] Y. Zhang, D. Y. Tzou, and J. K. Chen, Micro-and nanoscale heat transfer in femtosecond laser processing of metals, arXiv:1511.03566.
[18] M. Torabi and K. Zhang, Multi-dimensional dual-phase-lag heat conduction in cylindrical coordinates: Analytical and numerical solutions, Int. J. Heat Mass Transfer **78**, 960 (2014).
[19] K. C. Liu and H. T. Chen, Analysis of dual-phase-lag heat conduction in cylindrical system with a hybrid method, Appl. Math. Model. **31**, 369 (2007).
[20] K. C. Liu, Numerical analysis of dual-phase-lag heat transfer in a layered cylinder with nonlinear interface boundary conditions, Comput. Phys. Commun. **177**, 307 (2007).
[21] C. Liu, B. Q. Li, and C. C. Mi, Fast transient thermal analysis of gold nanoparticles in tissue-like medium, IEEE Trans. Nanobiosci. **8**, 271 (2009).
[22] A. H. Akbarzadeh and Z. T. Chen, Transient heat conduction in a functionally graded cylindrical panel based on the dual phase lag theory, Int. J. Thermophys. **33**, 1100 (2012).
[23] J. Zhou, Y. Zhang, and J. K. Chen, An axisymmetric dual-phase-lag bioheat model for laser heating of living tissues, Int. J. Thermal Sci. **48**, 1477 (2009).
[24] B. Mochnacki and M. Ciesielski, Micro-scale heat transfer. Algorithm basing on the control volume method and the identification of relaxation and thermalization times using the search method, Computer Methods Mater. Sci. **15**, 353 (2015).
[25] M. Ciesielski, Application of the alternating direction implicit method for numerical solution of the dual phase lag equation, J. Theor. Appl. Mech. **55**, 839 (2017).
[26] S. Saedodin, M. Torabi, H. Eskandar, and M. Akbari, Analytical and numerical solution of non-Fourier heat conduction in cylindrical coordinates, J. Comput. Anal. Appl. **13**, 411 (2011).
[27] B. Mochnacki and E. Majchrzak, Numerical model of thermal interactions between cylindrical cryoprobe and biological tissue using the dual-phase lag equation, Int. J. Heat Mass Transfer **108**, 1 (2017).
[28] W. Dai, L. Shen, R. Nassar, and T. Zhu, A stable and convergent three-level finite difference scheme for solving a three-dimensional dual-phase-lagging heat transport equation in spherical coordinates, Numer. Heat Transfer, Part B **46**, 121 (2004).
[29] A. Mukherjee, A. Lahiri, and S. C. Mishra, Analyses of dual-phase lag heat conduction in 1-D cylindrical and spherical geometry–An application of the lattice Boltzmann method, Int. J. Heat Mass Transfer **96**, 627 (2016).
[30] A. Lahiri, IIT Guwahati, Master of Technology project report, Numerical study of microscale conduction heat transfer with or without collimated laser irradiation, 2016.
[31] J. M. McDonough, I. Kunadian, R. R. Kumar, and T. Yang, An alternative discretization and solution procedure for the dual phase-lag equation, J. Comput. Phys. **219**, 163 (2006).
[32] M. Xu, J. Guo, L. Wang, and L. Cheng, Thermal wave interference as the origin of the overshooting phenomenon in dual-phase-lagging heat conduction, Int. J. Thermal Sciences **50**, 825 (2011).
[33] D. Jou and M. Criado-Sancho, Thermodynamic stability and temperature overshooting in dual-phase-lag heat transfer, Phys. Lett. A **248**, 172 (1998).
[34] T. N. Mishra, S. Sarkar, and K. N. Rai, Numerical solution of dual-phase-lagging heat conduction model for analyzing overshooting phenomenon, Appl. Math. Comput. **236**, 693 (2014).
[35] X. Li, M. Xu, and D. M. Christopher, Influence of size effect and boundary condition on temperature overshooting in nanoscale thermal conduction, Chin. Sci. Bull. **59**, 1334 (2014).
[36] M. A. Al-Nimr, M. Naji, and S. Al-Wardat, Overshooting phenomenon in the hyperbolic heat conduction model, Jpn. J. Appl. Phys. **42**, 5383 (2003).
[37] J. Y. Lin and H. T. Chen, Numerical solution of hyperbolic heat conduction in cylindrical and spherical systems, Appl. Math. Model. **18**, 384 (1994).
[38] G. Lebon, Heat conduction at micro and nanoscales: A review through the prism of Extended Irreversible Thermodynamics, J. Non-Equilib. Thermodyn. **39**, 35 (2014).
[39] Y. Dong, B. Y. Cao, and Z. Y. Guo, Temperature in nonequilibrium states and non-Fourier heat conduction, Phys. Rev. E **87**, 032150 (2013).
[40] J. Casas-Vazquez and D. Jou, Nonequilibrium temperature versus local equilibrium temperature, Phys. Rev. E **49**, 1040 (1994).
[41] H. Askarizadeh, E. Baniasadi, and H. Ahmadikia, Equilibrium and non-equilibrium thermodynamic analysis of high-order dual-phase-lag heat conduction, Int. J. Heat Mass Transfer **104**, 301 (2017).
[42] D. Y. Tzou and K. S. Chiu, Temperature-dependent thermal lagging in ultrafast laser heating, Int. J. Heat Mass Transfer **44**, 1725 (2001).
[43] D. Y. Tzou, *Macro-to Microscale Heat Transfer: The Lagging Behavior* (Taylor & Francis, Washington, DC, 1996).
[44] K. Ramadan, W. R. Tyfour, and M. A. Al-Nimr, On the analysis of short-pulse laser heating of metals using the dual phase lag heat conduction model, J. Heat Transfer **131**, 111301 (2009).
[45] L. G. Hector, Jr., K. Woo-Seung, and M. N. Ozisik, Propagation and reflection of thermal waves in a finite medium due to axisymmetric surface sources, Int. J. Heat Mass Transfer **35**, 897 (1992).
[46] M. F. Modest, *Radiative Heat Transfer* (Academic, New York, 2013).
[47] B. R. Barron and W. Dai, A hybrid FE-FD scheme for solving parabolic two-step micro heat transport equations in an irregularly shaped three-dimensional double-layered thin film, Numer. Heat Transfer, Part B **49**, 437 (2006).
[48] A. A. Mohamad, Lattice Boltzmann method for heat diffusion in axis-symmetric geometries, Prog. Comput. Fluid Dyn. **9**, 490 (2009).
[49] S. Succi, *The Lattice Boltzmann Method for Fluid Dynamics and Beyond* (Oxford University Press, New York, 2001).
[50] S. V. Patankar, *Numerical Heat Transfer and Fluid Flow* (CRC, Boca Raton, 1980).
[51] F. X. Alvarez and D. Jou, Memory and nonlocal effects in heat transport: From diffusive to ballistic regimes, Appl. Phys. Lett. **90**, 083109 (2007).
[52] V. K. Pustovalov, Theoretical study of heating of spherical nanoparticle in media by short laser pulses, Chem. Phys. **308**, 103 (2005).
[53] X. Liu, H.-j. Chen, X. Chen, C. Parini, and D. Wen, Low frequency heating of gold nanoparticle dispersions for non-invasive thermal therapies, Nanoscale **4**, 3945 (2012).